Universidad Carlos III de Madrid

Bachelor's Degree in Aerospace
Engineering
2016/2017

Bachelor Thesis
AWACS Static Loads Assessment

Alejandro Muñiz Luis

Tutor
Javier Hilario Montes

Leganés - 10th July 2017

This page intentionally left blank.

"Here's to the crazy ones. The misfits. The rebels. The troublemakers. The round pegs in the square holes. The ones who see things differently. They're not fond of rules. And they have no respect for the status quo. You can quote them, disagree with them, glorify or vilify them. About the only thing you can't do is ignore them. Because they change things. They push the human race forward. And while some may see them as the crazy ones, we see genius. Because the people who are crazy enough to think they can change the world, are the ones who do."

Steve Jobs (1955-2011)

This page intentionally left blank.

Abstract

Airborne Warning and Control System AWACS radars has become critical for succeeding in a wide range of military missions. The tactical and surveillance systems rely on the coverage and location of the radar antenna which can take several configurations.

The thesis is aimed to develop specific methods for obtaining the conceptual and preliminary loads of an AWACS lenticular dome and its two supporting struts mounted on the rear fuselage of an existing version of a civil or military aircraft. The flight loads are the result of the contributions of the aerodynamic and inertial loads evaluated in accordance with the FAR-25 and CS-25 regulations. For this purpose, an aerodynamic model of the radar is developed with the aid of a CFD software. Finally, the impact of the incremental loads over the rear fuselage is assessed.

This page intentionally left blank.

Contents

List of Figures

List of Tables

List of Symbols

Greek symbols

α	Aicraft Angle of Attack
β	Aicraft Sideslip Angle
δ	Control Surface Deflection
δ_R	Rudder Deflection
ϵ	Upwash
η	Dynamic Pressure Ratio Q/Q_{inf}
Γ	Wing Dihedral Angle
λ	Taper Ratio
μ	Dynamic viscosity
ν	Kinematic Viscosity
$\vec{\omega}$	Angular Speed Vector
ϕ	Bank Angle
ρ	Density
σ	Air Density Ratio ρ/ρ_{SL}
σ	Sidewash
τ	Engine Thrust Factor
τ_{wall}	Wall Shear Stress
θ	Pitch Angle

Indices

ac	Aircraft
app	Approach
$centr$	Centrifugal

cg	Centre of Gravity
d	Dome
eng	Engine
fus	Fuselage
h	Horizontal Tail-Plane
i	Inertial
ind	Induced
max	Maximum
$mill$	Wind-milling
min	Minimum
OEO	One-Engine-Out
ref	Reference
SL	Sea Level
st	Strut
v	Vertical Tail-Plane
w	Wing
$xwind$	Cross-wind

Latin symbols

$\dot{p}$	Rolling Angular Acceleration
$\dot{q}$	Pitching Angular Acceleration
$\dot{r}$	Yawing Angular Acceleration
$\overrightarrow{a_z}$	Vertical Acceleration Vector
AR	Aspect Ratio
b	Span
C_D	Drag Coefficient $\frac{D}{QS}$
C_f	Skin Frictional Coefficient
C_{L_α}	$\frac{\partial C_L}{\partial \alpha}$
C_L	Lift Coefficient $\frac{L}{QS}$
C_l	Moment around X-axis $\frac{M_x}{QSD}$

C_m	Moment around Y-axis $\frac{M_y}{QSD}$
C_n	Moment around Z-axis $\frac{M_z}{QSD}$
C_p	Pressure Coefficient $\frac{P-P_\infty}{1/2\rho V^2}$
C_r	Root Chord
C_T	Thrust Coefficient $\frac{T}{QS}$
C_x	X-Force Coefficient $\frac{F_x}{QS}$
C_y	Y-Force Coefficient $\frac{F_y}{QS}$
C_z	Z-Force Coefficient $\frac{F_z}{QS}$
D	Diameter
D	Drag Force
F	Force or Load
f	Frequency
F_A	Aerodynamic Force
F_T	Thrust Force
g	Gravity Acceleration
H	Height
I	Tensor of Inertia
k	Von-Karman Constant
L	Lift Force
M	Mach number
m	Mass
M_C	Design Mach Cruising Speed
M_D	Design Mach Diving Speed
N_x, N_y, N_z	Load Factors for each Reference Axis
p	Rolling Angular Speed
Q	Dynamic Pressure ($1/2\rho V^2$)
q	Pitching Angular Speed
R	Engine Bypass Ration

r	Yawing Angular Speed
Re	Reynolds number
S_d	Dome Planform Surface
S_{ref}	Reference Surface or Wing Surface
T	Thrust
u	Local Longitudinal Velocity
U_τ	Frictional Velocity
V	Velocity
v	Local Lateral Velocity
V_A	Design Manoeuvring Speed
V_C	Design Cruising Speed
V_D	Design Diving Speed
V_S	Stall Speed
V_{EAS}	Equivalent Air-Speed
V_{S1}	Stall Speed at 1g
V_{TAS}	True Air-Speed
W	Weight
w	Local Vertical Velocity
x	Distance in the X-axis
y	Distance in the Y-axis
y^+	Wall Non-dimensional Distance
z	Distance in the Z-axis

List of Abbreviations & Acronyms

ADB	Aerodynamic Database
AEW&C	Airborne Early Warning and Control
APU	Auxiliary Power Unit
AWACS	Airborne Warning and Control System
CAD	Computer Aided Design
CFD	Computational Fluid Dynamics
CG	Centre of Gravity
CS	Certification Specifications
CRI	Certification Review Item
EAS	Equivalent Air-Speed
EASA	European Aviation Safety Agency
FAA	Federal Aviation Administration
FAR	Federal Aviation Regulations
FEM	Finite Element Method
FY	Fiscal Year
ISA	International Standard Atmosphere
KEAS	Knots Equivalent Air-Speed
KEAS	Knots Equivalent Air-Speed
LH	Left Hand-side
NACA	National Advisory Committee for Aeronautics
NATO	North Atlantic Treaty Organization
OEO	One Engine Out
OEW	Operating Empty Weight
RH	Right Hand-side
RMS	Root Mean Square
TAS	True Air-Speed
TLAR	Top-Level Aircraft Requirements
VTP	Vertical Tail-Plane

Chapter 1

Introduction

1.1 Motivation

The Airborne Warning and Control System, AWACS, is a tactical and all-weather surveillance military system. It encloses the ability to fit radar antennae and navigation systems into an aircraft for communication and surveillance purposes. Nowadays, these type of aircraft are used to manage all sort of air, ground and maritime assets as well as to have battlefield controllability and decision-taking abilities. With the evolution of electronics and technology, the use of AWACS systems has became critical for succeeding at a wide range of military missions.

Throughout history, there have been different models of AWACS antennae. Among them, the lenticular dome mounted over the fuselage stands out for being the one with the largest coverage due to its shape and place, Figure 1.1. This specification is key to achieve tactical superiority.

In engineering terms, it is important to be able to quantify the impact of such an aircraft configuration. At the conceptual design phases, the information related to the design may be limited and there will be no FEM models to rely on, therefore, it is useful to count on general methods in order to assess the loads and aerodynamic effects over the aircraft structures.

This bachelor thesis focuses on the development of specific tools to estimate the conceptual and preliminary loads of a lenticular antenna of an AWACS system to be installed in a derivative version of a wide-body civil aircraft. The most relevant loads are those associated to the emergency landing conditions, flight manoeuvres, gusts and dynamic landing. However the last two of them require a detailed structural model to be analysed and this is out of the scope of this project. The goal of this thesis is to develop a preliminary design handbook for the estimation of the static loads and its comparison with any ulterior result.

Figure 1.1: *Boeing E3-Sentry AWACS aircraft [22]*

1.2   Background

The structural loads analysis involves the calculation of the loads, deformations or accelerations acting on the aircraft structure for flight manoeuvres, flight in turbulence, landing, and ground-handling conditions [31]. The loads cause stresses, displacements and overloading situations in structures which may lead to failures. Therefore, a correct assessment must be considered for design purposes.

In general, the loads can be classified according to three criteria:

(i)   The recurrence in the aircraft life-time, this is, how frequently the loads are encountered:

   (a)   Check-stress or design loads - which include:
- Limit loads - the maximum loads expected in service.
- Ultimate loads - the limit loads multiply by a prescribed factor of safety, usually 1.5 .

   (b)   Fatigue loads - loads lower than the design loads but encounter more frequently in the normal operations of the aircraft.

(ii)   Aircraft operational phase they are found:

- Flight loads
- Ground loads

(iii)   The structural response related to the frequency content of the loads:

- Static loads - loads whose magnitude, direction and point of application do not change (or the change is very slow) in time, usually for frequencies $f << 1$ Hz.
- Dynamic loads - loads whose magnitude, direction or point of application do change in time, usually with a frequency of variation $f > 1$ Hz.

Figure 1.2: *Loads according to its recurrence in the aircraft life-time*

Table 1.1: Loads' classification according to the operational phase and the structural response

	Operational Phase	
Structural Response	**Ground**	**Flight**
Static	Jacking cases Ground handling	Flight manoeuvres One-Engine-Out conditions
Dynamic	Dynamic landing Taxiing Landing in unpaved runways	Discrete tuned gust Continuous turbulence Buffet

Static Loads' Models

Loads' models are analytical tools to infer the forces and moments the structure will experience under any condition. These models are always validated by flight tests. In the field of static loads, the integrated forces and moment distribution for the whole aircraft are the result of the sum of loads coming from two different models:

- Aerodynamic model
- Inertial model

Aerodynamic model

The aerodynamic model is based on the distribution of aerodynamic forces and moments along the aircraft elements. The model is built linearly dependent to some aerodynamic variables such as the incidence angle α, the sideslip angle β, the control surface deflections δ, the non-dimensional angular velocities $\hat{p}, \hat{q}, \hat{r}$, or the thrust coefficient C_T. Besides, a unique model should be formulated for each combination of Mach number, height and flap configuration considered.
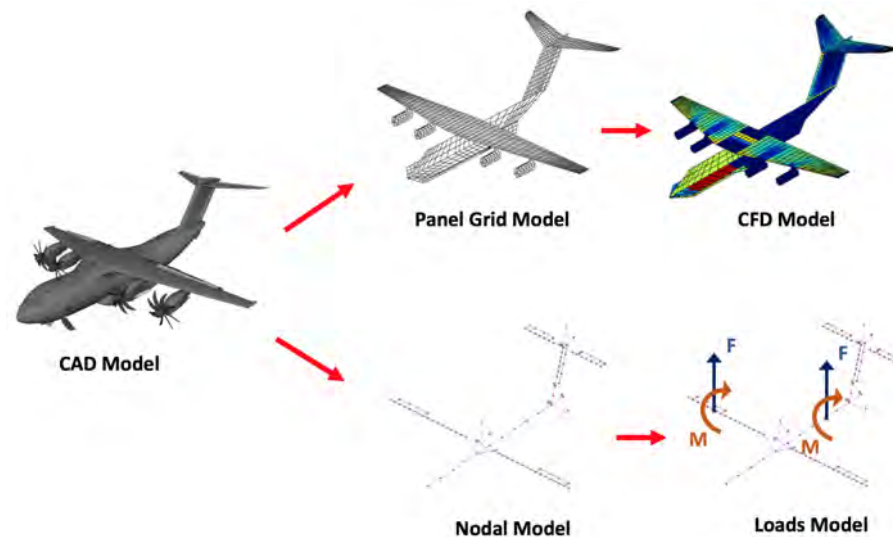
Figure 1.3: *Aerodynamic model - loads distribution methods [11]*

The distribution of aerodynamic loads may be accomplished by two methods:

- Pressure distribution on grid panels
- Loads along nodal points

The pressure distribution in panels is the result of CFD simulations. The aerodynamic surfaces are discretised into a definite number of grid panels where the local pressure coefficient is computed. Besides, the pressure distribution may be corrected with data from wind tunnel tests and the Aerodynamic Database (ADB) of the aircraft.

The second approach is to provide the aerodynamic loads distributed along nodal points in the aircraft reference lines. For instance, the forces and moments may be given along the fuselage reference line or the chord line for the wing.

Inertial model

The inertial model retains the inertial and gravitational effects of the aircraft. For this purpose, an accurate mass model distribution is required to integrate the loads along the different parts of the aircraft. As shown in Figure 1.4, each part is discretised into a finite number of elements or nodes where masses are concentrated and loads computed.

In terms of variables, the equation for the inertial forces and moments are expressed as a function of 12 variables which constitute the inertial variables of the model. These are:

- 3 load factors: N_x, N_y, N_z
- 3 angular accelerations: $\dot{p}$, $\dot{q}$, $\dot{r}$
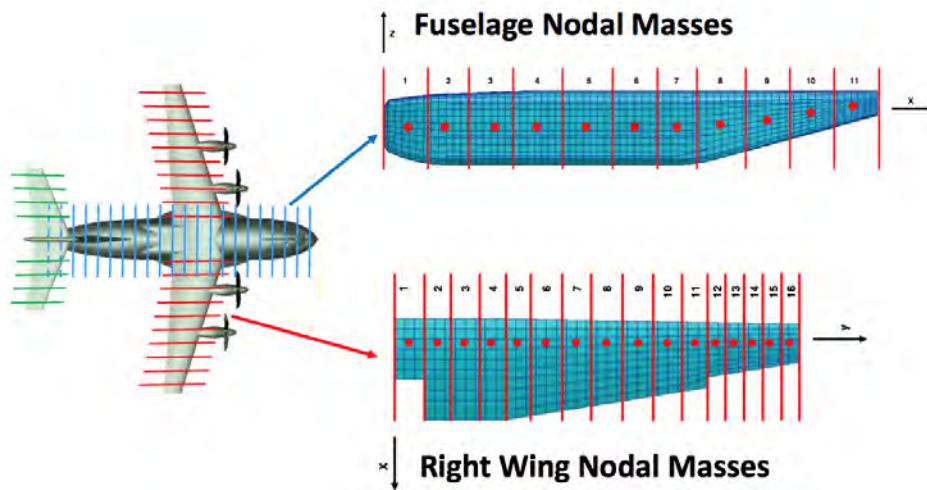
Figure 1.4: *Inertial model - nodal mass distribution [11]*

- 6 product of angular velocities: p^2, q^2, r^2, pq, pr, qr

The inertial loads equations are detailed in Section 4.3.2.

1.3 Legal framework

Safety must be ensure in aviation through the development of procedures and the implementation of regulations. There are two organizations in charge of setting them: EASA and FAA.

EASA is the European aviation authority created in 2002 by the European Commission; while the FAA is the Civil Aviation Authority of the United States of America. Although both agencies dictates their own regulations, they tend to agree on the same standards which are mostly apply worldwide. Therefore, FAR-25 regulations about strength are very similar to the CS-25 by EASA.

As the thesis is focused on a turbofan aircraft, the applied civil regulations are the EASA Certification Specifications for Large Aeroplanes CS-25 (Mass > 5700 kg); and the FAA Federal Aviation Regulations FAR-25 corresponding to "Airworthiness Standards for transport category airplanes". Specifically, Subpart C of both regulations is related to calculation of loads.

Concerning the applicability to the calculation of static loads, both regulations establish general and manoeuvring requirements. The general requirements applicable to the AWACS are specified by the following regulations:

- 25.301 Loads
- 25.303 Factor of Safety
- 25.305 Structure and deformation
- 25.321 General
- 25.333 Flight manoeuvring envelope
- 25.335 Design airspeeds
- 25.337 Limit manoeuvring load factors

And the aircraft manoeuvring conditions applicable to the AWACS, without considering gust loads, are defined by:

- 25.331 Symmetric manoeuvring conditions
- 25.349 Rolling conditions
- 25.351 Yaw manoeuvre conditions
- 25.367 Unsymmetrical loads due to engine failure conditions

CS/FAR-25.301(a) dictates that the strength requirements are provided in terms of limit loads unless otherwise prescribed. Limit loads are the maximum loads expected in service and must not involve any structural permanent deformation. On the other hand, ultimate loads are defined as the limit loads multiplied by a factor of safety and must be withstand without structural failure. Both loads are used for structural design purposes depending on the conditions examined. For instance, at nominal flight conditions the loads are limit, however ultimate loads are considered for emergency landing conditions.

According to CS/FAR-25.303, the factor of safety applied to the external limit loads is 1.5 unless the strength requirements are specified in terms of ultimate loads where no factor is needed. This value was established in 1933 by the National Advisory Committee for Aeronautics (NACA) and it remains constant since then. The goal of this factor is to account for some inaccurate assumptions in the mechanical properties of the structure, possible manufacturing errors and uncertainties in the loads' models.

1.4   Scope of the work

The thesis focuses on developing specific methods to compute the preliminary and conceptual loads of an AWACS lenticular dome. The aim is to design a radar to be mounted on an existing civil aircraft, in this case the Airbus A330-200, and to evaluate the impact of the radar over the fuselage in terms of loads in accordance with FAR-25 and CS-25 regulations.

The main assumptions of the project concerns the loads' calculation:

- In terms of operational conditions, only static loads from flight manoeuvres are considered. Therefore, regarding the radar, just an aerodynamic model and inertial model are required.

- No aeroelastic effects are taken into account, in other words, the dome and struts are assumed to be rigid. This assumption is considered to be in close proximity to the actual structure since the radar is required to keep as horizontal as possible for the correct operations of the radar.

The document is divided into six chapters which are succinctly presented below:

- Chapter 2 is dedicated to review the history of AWACS aircrafts from the first aeroplanes to the current state of the art. The most important AWACS configurations are analysed and their advantages and disadvantages stated. Finally, a statistical study is performed on current dome-shape AWACS to extract the trends in their designs

- Chapter 3 is devoted to explain the setup of the CFD simulation. This chapter presents the CAD model, the computational domain, boundary conditions and mesh grid used for this purpose.

- Chapter 4 introduces the aerodynamic and inertial model developed for the radar. The aerodynamic model is inferred from the numerical results obtained in Chapter 3 by performing a regression analysis. Moreover, the inertial model is calculated with mass data from a previous AWACS radar and the aid of a CAD software.

- Chapter 5 outlines the flight requirements applicable for the static loads' calculation, which are mandated by the EASA and FAA authorities. The flight conditions are explained and the radar loads are presented.

- Chapter 6 includes an analysis of the fuselage loads. Specifically, it evaluates the radar impact on the loads of the rear fuselage structure and the side-wash effect over the vertical tail.

Finally, some conclusions are drawn and the main ideas of the project are outlined.

Chapter 2

AWACS in history

2.1   First AWACS in history

The concept of an aerial vehicle with the purpose of managing all sort of actuations goes back to 1794 with the figure of Captain Jean-Marie-Joseph Coutelle. He was a French engineer and pioneer in charge of building balloons to help the French Revolutionary Army to success.

In modern history, the concept dates back to the early 1940's, when the Royal Air Force used high-altitude aircraft observers to aid into the tactical decisions of ground troops. It was only after the development of electronics and avionics that this result in new type of military aircrafts with the goal of disrupting the course of a war. The first known prototype mounted a rotating antenna into a Vickers Wellington bomber as a system for detecting the German long range Focke-Wulf Fw-200 Condors which threatened to bomb ships along the West coast of Great Britain during World War II.

Figure 2.1: *Vickers Wellington bomber [53]*

Figure 2.2: *Detail view of the Vickers Wellington rotating antenna [24]*

Later, in 1944, the U.S. Navy started the development of a radar system with a range of 100 miles to be carried in a TBM Avenger. This bomber served as a test for the production of the widely-used Lockheed EC-121 "Warning Star" in the Vietnam War until retired in 1982.

The Soviet Union also developed their own early-warning aircraft models during the Cold War Era. In 1965 entered in-service the so-called Tu-126, a
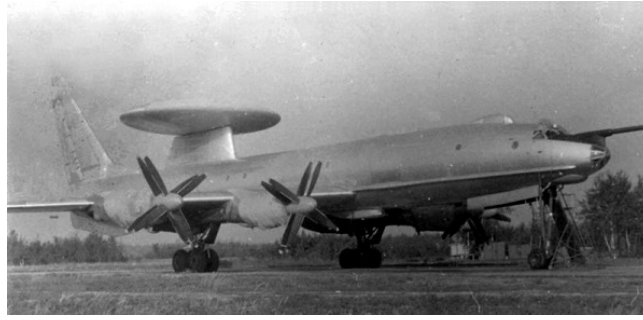
Figure 2.3: *Tupolev Tu-126 with rotative dome [46]*

version of the four turboprop Tupolev Tu-114 fitted with a rotative dome of 11 meters in diameter and a refuelling probe to extend its endurance capability up to 20 hours. This aircraft remained in-service until its substitution in 1984 by a new generation of AWACS, the Ilyushin Il-76 and its current version, the Beriev A-50, which participated in the recent Syrian Civil War.

Moreover, blimps have also carried AEW&C systems. The American class-N blimps were very appropriated for the task due to the huge endurance capabilities, over 200 hours, but accidents discouraged their use around the world during the 1950's and 1960's.

2.2   State of the art

The inventiveness of aeronautical engineers has played a big role on the different shapes of the AWACS radars throughout history. The need to accommodate radar antennas on existing aircrafts gave rise to original configurations such as rotodomes, dorsal beams or bulbs that vary according to the aircraft capabilities, the weight and the required range coverage. In this section, the current most relevant configurations are reviewed.

Nowadays there exist several nations with AWACS capabilities among their fleet. The most significant of those aircrafts has been the American E-2C Hawkeye and the Boeing E3-Sentry that proved to be a valuable asset for early threat detections during important military operations in the Gulf War and Iraq War respectively. Both of them incorporate a dome-shaped radar.

The Northtrop Grumman E-2C Hawkeye, shown in Figure 2.4, is a twin-turboprop aircraft specifically developed in the late 1950's for surveillance missions. It was conceived with a folded wing aimed to have carrier capabilities for the Navy and its design stands-out by the large dome diameter of 7.32 meters hold by six struts. The empennage mounts a twin vertical tail at the end of the horizontal stabilizers to keep the tails from interfering with the look-down capabilities of the antenna [51] and to meet the size constrictions of a carrier storage.

The Boeing E3-Sentry is the 'big-brother' of the E-2C Hawkeye. It is a long-range 4-engine turbofan with the most innovative communication and surveillance technology. The E3 is based on a Boeing 707-320 aircraft first

Figure 2.4: *Northtrop Grumman E-2C Hawkeye [41]*

Figure 2.5: *KJ-2000 [55]*

Figure 2.6: *Nimrod AEW3 [1]*

Figure 2.7: *Boeing EB-707 [18]*

Figure 2.8: *Saab-340 AEW&C [26]*

Figure 2.9: *Embraer E-99 AEW&C [15]*

Figure 2.10: *Westland AEW SH-3 Sea King [6]*

Figure 2.11: *Kamov Ka-31 [39]*

delivered in 1976 to the United States Air Force. Now the system is operated by the NATO organization, Saudi Arabia, the United Kingdom and France.

The antenna mounted on top is a rotating dome of 9.11 meters in diameter supported by two struts which covers an area of 500,000 km^2 around the aircraft or more than 400 km in all directions, 360° degrees of azimuth, including low flying aircrafts [35]. This capabilities are delivered by a slotted planar array antenna, see Figure 2.12, with a high pulse Doppler waveform technology which is able to identify targets over the horizon. The endurance of the missions is constrained to 22 hours, including in-flight refuelling, due to engine oil limitations and it is operated by a crew of 19-21 people.

Figure 2.12: *Radar array inside dome structure [21]*

The strut configurations must withstand a dome of more than 13,000 lbs. From the stress point of view, the twin-strut configuration is structurally more demanding than the six-strut configuration of the E-2C Hawkeye. However, the drag increment produced by the latter one penalised the endurance capabilities [9]. This is why, for dome-like shapes the twin-strut configuration is the preferred option in turbofan aircrafts whose cruise speed is closed to Mach 0.8.

Moreover, China has also developed a domestic AWACS dome, the KJ-200 shown in Figure 2.5, which is a modified version of the Russian Ilyushin Il-76 aircraft. The airframe mounts a phased array radar inside a non-rotating dome with three antennas placed 120° apart in a triangular shape.

Other AWACS configurations are the dorsal beam mounted on top of the fuselage or the front/lateral bulbs.

The beam-shape configuration are used by the governments of Brazil, Turkey, Sweden and India because they represent a cheaper alternative to the radar domes. The advantages are the light weight of the radar ($\sim$900 kg) and the streamline shape, which decreases the weight to drag ratio. Therefore, it is more convenient for smaller airframes such as the Swedish Saab-340 AEW&C or the Brazilian Embraer E-99 shown in Figures 2.8 - 2.9 respectively. Nevertheless the drawback of the beam is the coverage, which reduces to 150° in azimuth for both sides. Besides, the endurance of the these small aircrafts is about 6 hours, which could fall short for some missions.

The third analysed configuration are the bulbs, which are frontal and lateral protrusions from the aircraft fuselage to accommodate the surveillance and communication equipments. The first model with bulbs was the British

11

Aerospace Nimrod, developed in the late 1960's by the United Kingdom from a modified version of the de Havilland Comet. Among the several versions, there was one with AEW&C capabilities, the Nimrod AEW3 shown in Figure 2.6, but the program was cancelled in 1986 in favour of the up-coming Boeing E3-Sentry.

Currently, the Chilean Air forces are the only one operating an aircraft like this, the Boeing EB-707 'Condor' in Figure 2.7. It is a modified version of a Boeing 707 with two lateral band-bulbs and a characteristic frontal protrusion. In general, the conformal antennas reduces the total drag compared to the other configurations but the main disadvantage is the costly modifications of the fuselage. Furthermore, the lateral antennas cover 120° each, thus two more antennas, at the front and the tail, are required to scan the remaining sections.

In summary, Table 2.1 compares the characteristics of the three types of radars analysed in this section.

Table 2.1: Comparison of radar characteristics

	Dorsal Beam	**Bulbs**[1]	**Dome**
Weight	Light	Heavy	Heavy
Drag Impact	Medium	Low	High
Coverage	120°	300°	360°
Fuselage Modification	Little	Costly	Little
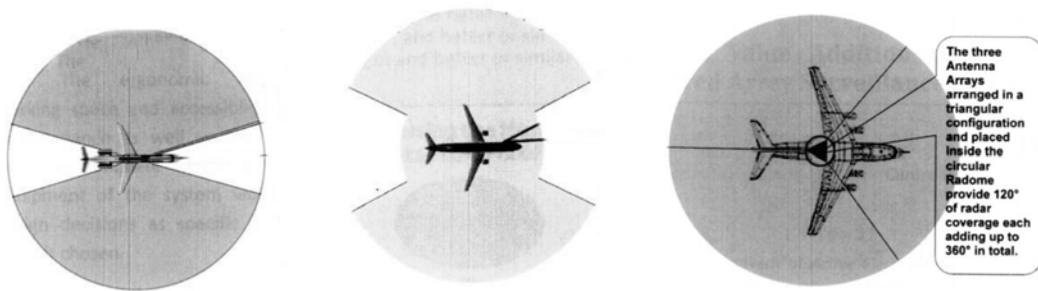
Figure 2.13: *Dorsal beam coverage*

Figure 2.14: *Bulbs coverage*

Figure 2.15: *Dome coverage*

Figures 2.13 - 2.15: Comparison of radar coverage for beam, bulbs and dome configurations, Christopher [10]

Moreover in the field of rotating-wing aircrafts, AEW&C helicopters represent a most affordable option for short mission deployments. The antennas may take different shapes as bulbs attached to a lateral or planar arrays folded under the frame. These systems are currently mounted by the Spanish Navy, operating a SH-3 Sea King or the Indian Navy in a Russian Kamov Ka-31, as pictured in Figures 2.10 - 2.11.

---

[1]Considering two lateral and one frontal bulb

2.3   Statistics in AWACS dome design

The first steps in designing an aircraft with a new configuration should be to undertake a historical survey of aircrafts within the same category. For this purpose statistical data from 7 different aircrafts with a dome mounted over the fuselage has been collected.

The list represents a database of AWACS-dome aircrafts including the first-known dome entered into service, the Northtrop Grumman E-2C Hawkeye shown in Figure 2.4, and the last aeroplane of this characteristics developed, the Airbus C-295 AEW shown in Figure 2.16.

The 7 aircrafts included in the survey are accompanied by the year of its first flight. Besides, an 8th aircraft is included as a red dot in the graph which constitutes the aeroplane chosen as example of application in this project.

1. Northtrop Grumman E-2C Hawkeye, 1960
2. Tupolev Tu-126, 1962
3. Boeing 707 E3 Sentry, 1976
4. Beriev A-50 AEW, 1978
5. Boeing E-767, 1994
6. KJ-2000 AEW, 2003
7. Airbus C-295 AEW, 2011
8. Airbus A330-200 - this is the aircraft where the radar of this thesis is analysed.

Figure 2.16: *Airbus C-295 AEW [12]*

In terms of common features, two of them have turboprop engines and the rest of them are turbofan. Four of the above have a high-wing configuration, and among them, two have T-tails and one H-tail. The remaining ones have conventional tails and low-wing configurations.

Regarding the radar, six of those listed hold the dome with a twin-strut configuration and the E-2C Hawkeye uses six struts.

The dome longitudinal location is behind the centre of gravity of the aircraft in all of them, specifically between the 50% and the 65% of the fuselage length as observed in Figure 2.17. The data indicates that correlation is poor in terms of fuselage length. The longitudinal location for the radar of this project is selected at 33 m., based on prior studies of the Airbus A330-200 to mount a radar. This value agrees with the fitting tendency of previous AWACS models.
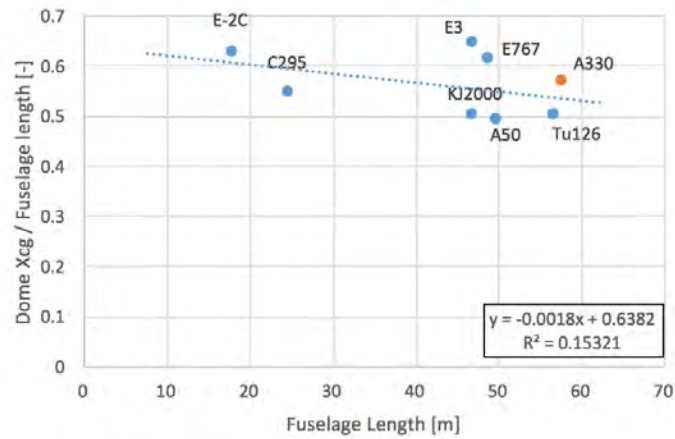
Figure 2.17: *Normalized dome longitudinal location versus the fuselage length*

Concerning the height of the dome above the fuselage, Figure 2.18 shows a comparison of the non-dimensional height with respect to the VTP span. There is a relative good correlation described by Equation (2.1) where the trend is to reduce the height of the dome in terms of the vertical tail span as the latter one increases. The range of heights is between 47% to 70% of the VTP span.

$$\frac{h_{dome}}{b_v} = 0.79 - 0.033b_v \qquad (2.1)$$
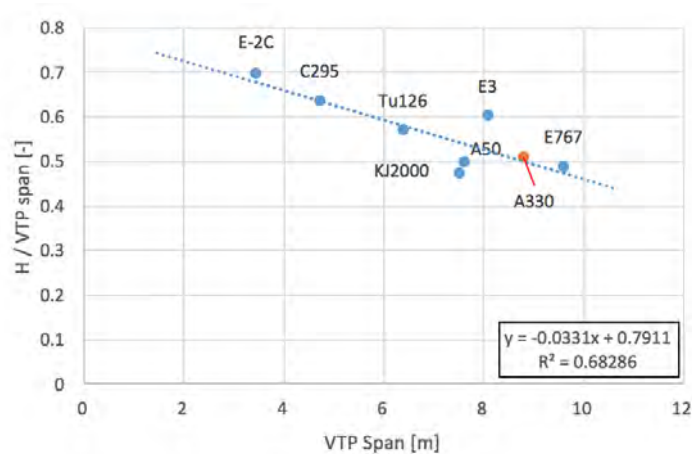
Figure 2.18: *Non-dimensional dome height versus the VTP span*

The diameter of the dome is reviewed in Figure 2.19. The measurement is normalized by the fuselage width and compared to it. The data show a good correlation for the turbofan aircrafts with the two turboprop being the outsiders, the E-2C and the C-295. The equation of the fitting line is:

$$\frac{D_{dome}}{W_{fus}} = 3.899 - 0.374 W_{fus} \tag{2.2}$$
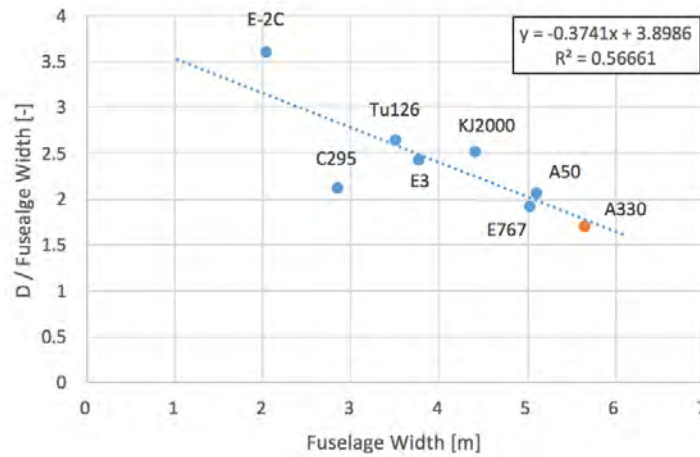
Figure 2.19: *Non-dimensional diameter versus the fuselage width*

The thickness of the dome is analysed in Figure 2.20 in terms of its aspect ratio, which is the ratio between the thickness and the diameter. Most of the domes are in the range of 0.15 to 0.2, where the highest ones are the Boeing E-767 and Boeing E3 Sentry while the lowest is the E-2C Hawkeye with 0.12. For this thesis, an aspect ratio of 0.2 is chosen.
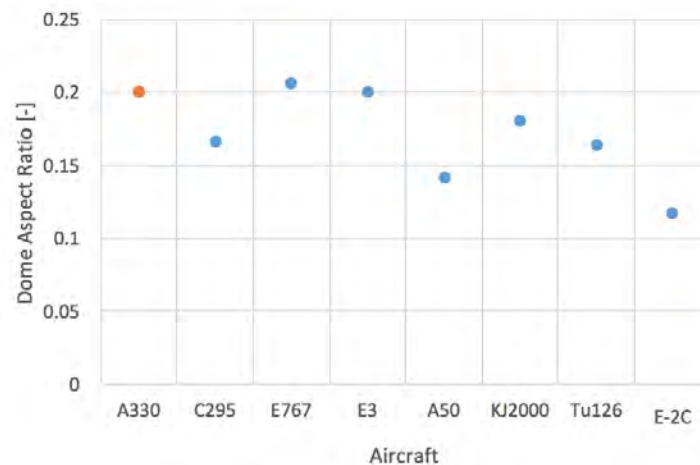
Figure 2.20: *Aspect ratio of the dome*

Chapter 3

CFD Simulation Setup

The CFD simulation is set to infer the aerodynamic model for the AWACS radar. In general, a CFD simulation requires the definition of four elements:

1. CAD design of the model to be tested
2. Computational Domain and boundary conditions
3. Mesh grid
4. Turbulence model

3.1   CAD Model

The radar is modelled in a Computer-Aided Design (CAD) software. The 3D model takes the dimensions from the E3-Sentry aircraft shown in Figure 3.1.

Figure 3.1: *Close-up view of the E3-Sentry radar [5]*

As seen in Figure 3.1 and 3.2, the radar assembly is composed by two parts mounted on a fuselage:
- Dome - designed as an oblate spheroid or ellipsoid of 9.144 meters in diameter.

- Struts - two struts hold the dome. They both have a symmetric 4-digit NACA airfoil, NACA-0012, and they are tilted 10° inwards from the vertical position.

16

Figure 3.2: *3D CAD design*

The dome is an axisymmetric body, with an ellipsoidal profile and an aspect ratio of 0.2 as picture in Figure 3.3. This is large enough to accommodate the required electronics for the AWACS system and still keep a good aerodynamic shape so the drag is minimized.

The struts are designed with a constant chord airfoil profile for the same reason. They have a chord of 1.715 meters, as shown in Figure 3.4 and a vertical height to the dome surface of 4.5 meters.

Appendix B contains the detail drawings of the model dimensions.
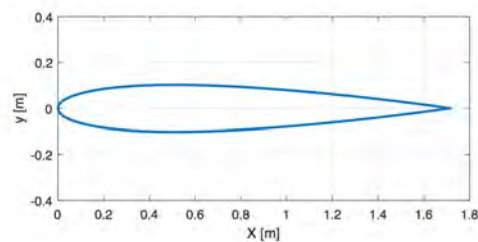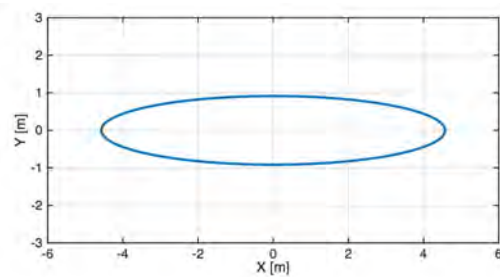
Figure 3.3: *Profile of the dome at the plane of symmetry*

Figure 3.4: *NACA-0012 Struts airfoil*

Figures 3.3 - 3.4: Dome profile and struts airfoil section

3.2   Computational Domain and Boundary Conditions

The computational domain is the space where the flow equation are solved and its size depends on the model being tested. The domain should be large enough to avoid fluid stream reflection at boundaries which leads to non-realistic pressure gradients.

Researchers have not agreed on a fixed distance, therefore they have been using arbitrary domain sizes, large enough to get accurate results but constrained by the computational cost. It is true that there exist a chance of unrealistic results if the computational region is expanded without an adequate grid spacing [52], but again, a convenient balance must be reached.

For this purpose, a grid sizing study is carried out to assess the extent of the boundaries and guarantee realistic flow solutions. For a given incidence $\alpha = 5^o$ and sideslip angle $\beta = 5^o$, the longitudinal force coefficient Cx is monitored for different depths, the side force coefficient Cy is monitored for several half-width extensions and the vertical force coefficient Cz is measured for increasing heights. All the values are normalised by the diameter of the dome and presented in Figures 3.5 - 3.7.
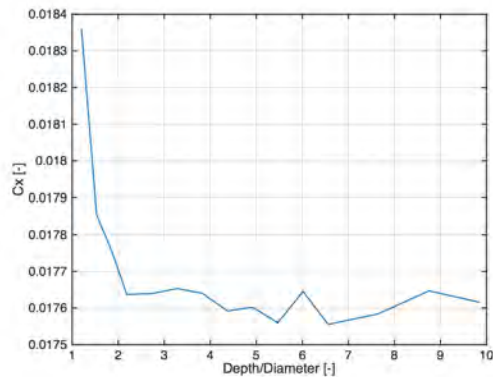
Figure 3.5: *Cx force versus the normalised depth*
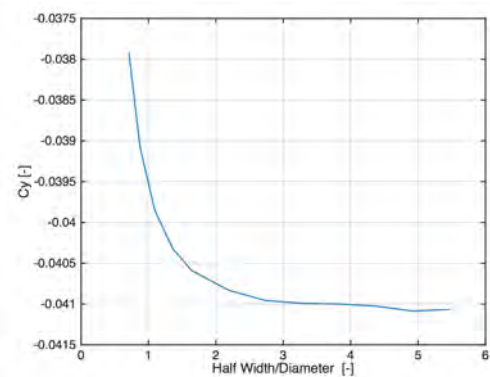
Figure 3.6: *Cy force versus the normalised half-width*
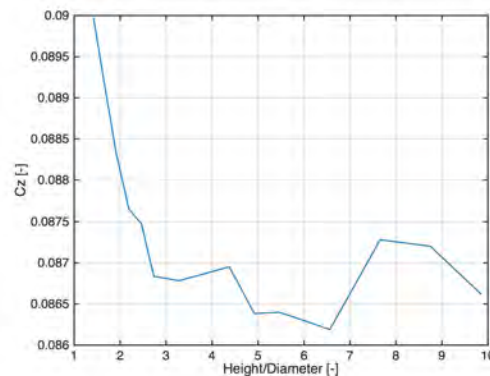
Figure 3.7: *Cz force versus the normalised height*
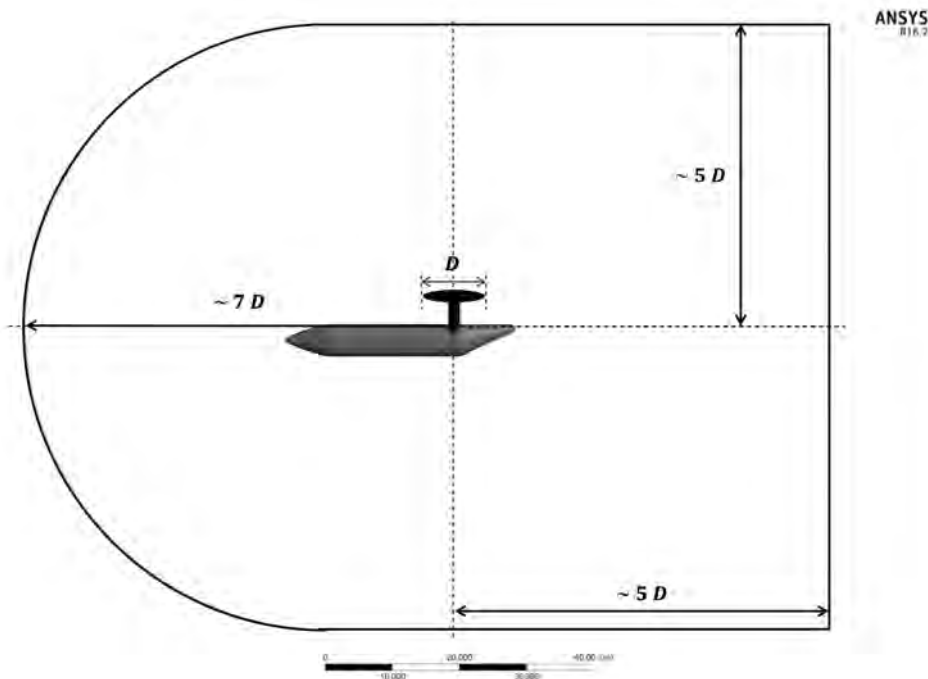
Figure 3.8: *Side-view of the computational domain*
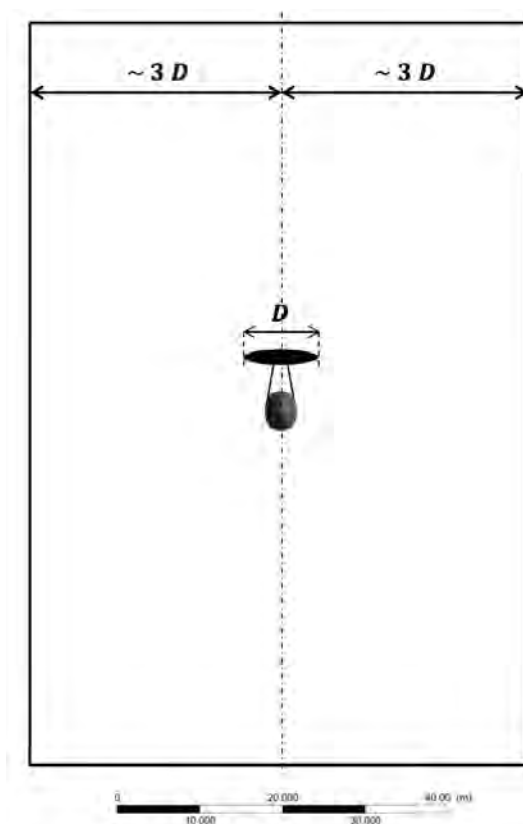
Figure 3.9: *Front-view of the computational domain*

Figures 3.8 - 3.9 show the nominal size of the domain used in the CFD simulation with a distance about $5D$ for the depth and height of the domain, and $3D$ for the lateral faces, where D is the diameter of the radar.

The boundary conditions for this experiment are set to a Mach number of $M = 0.2$ at sea level, therefore, the air inlet velocity is 68.05 m/s related to a Reynolds number of $4.19 \cdot 10^7$. The air is modelled as an ideal gas whose fluid properties vary as a function of the temperature. Its density ρ_{air} and dynamic viscosity μ_{air} are set to $1.225\ kg/m^3$ and $1.8205 \cdot 10^{-5}\ kg/(m \cdot s)$ respectively according to the International Standard Atmosphere (ISA) model and a static pressure of 1 atm. The roof, floor, side-walls and outlet are specified as *Openings* with a relative pressure of zero. The radar and fuselage surfaces are modelled as a *non-slip wall* condition with smooth roughness and adiabatic properties.

3.3   Meshing

Most of the time invested in a Computational Fluid Dynamics (CFD) project is devoted to the generation of a mesh for the domain which fulfils the trade-off between accuracy and solution costs.

The usual procedure to assess the accuracy of the mesh is to run several cases with different mesh sizes and check whether the numerical solution converges. This is called a grid-independence study and it is considered a bottleneck in the CFD process.

The limitations of the computational resources in these experiment represent the main constraint of the quality and density of the mesh used.

3.3.1   Grid

When it comes to meshing, there exist two different types of grids: structured and unstructured. The idea behind each type of grid is the same, the division of the full domain into a large number of elements or cells so the equations are solved for each element in relation to the surrounding ones. The difference between them is found on the way they are distributed. The structured mesh is usually divided into cuboid elements arranged in

Figure 3.10: *Control volume definition [4]*

rows and columns so the mesh grid takes longer to be built, however the convergence and the speed of the simulation are improved. On the other hand, the unstructured mesh is made out of tetrahedral elements that are

easy to fit around complex surfaces, as the ones in the aerospace industry, nevertheless the convergence and computational time are not as good as for a structured mesh and the number of elements tend to significantly increase.

ANSYS CFX 16.2 uses an element-based finite volume method originally developed by Schneider and Raw in 1987. The grid is used to discrete the domain into a finite number of volume cells although the flow properties are stored at each node. A two dimensional illustration is shown in Figure 3.10 but the three dimensional concept would be the same. The control volume, the shaded area, is constructed around each node by joining the midpoint of the edges surrounded the node and the elements centres. Therefore, the accuracy depends on the number of nodes of the mesh rather than the number of elements as it is usually believed for a finite volume approach.

In this thesis project, the grid is a mono-block mesh conformed by tetrahedral elements and prism extrusions near the wall with a C-grid topology. The presence of the wall surface demands small grid spacings to deal with the steep profile gradients in the boundary layer, therefore, an inflation layer of elongated prisms, with aspect ratios up to ~ 300, is built in order to maintain the flow properties in the longitudinal direction. The total number of nodes is $1.5 \cdot 10^6$ which corresponds to $6 \cdot 10^6$ of cells.

3.3.2   Grid Refinement Regions

Grid refinement regions are defined inside the computational domain to improve the convergence and mesh quality in certain areas. These regions are either around a wall where the boundary layer demands smaller grid spacing without compromising the cell quality, for instance, around the struts; or regions which are known for having significant gradients in the flow solutions, for example, behind the radar where a downwash is created.

Three refinement regions are created inside the domain as displayed in Figure 3.11:

1. Refinement around the fuselage and the dome
2. Two thin rectangular prisms around the struts
3. Downwash region

3.3.3   Mesh Sensitivity Study

A mesh sensitivity study quantifies the accuracy of a finer grid when compared to a coarser one. That means, it is a measure to check that the solution does not vary significantly if the mesh is further refined. On top of that, a finer mesh implies higher computing time because the number of nodes to be solved increases. Thus the grid study represents a good approach to find the optimal balance between solution accuracy and computational costs.
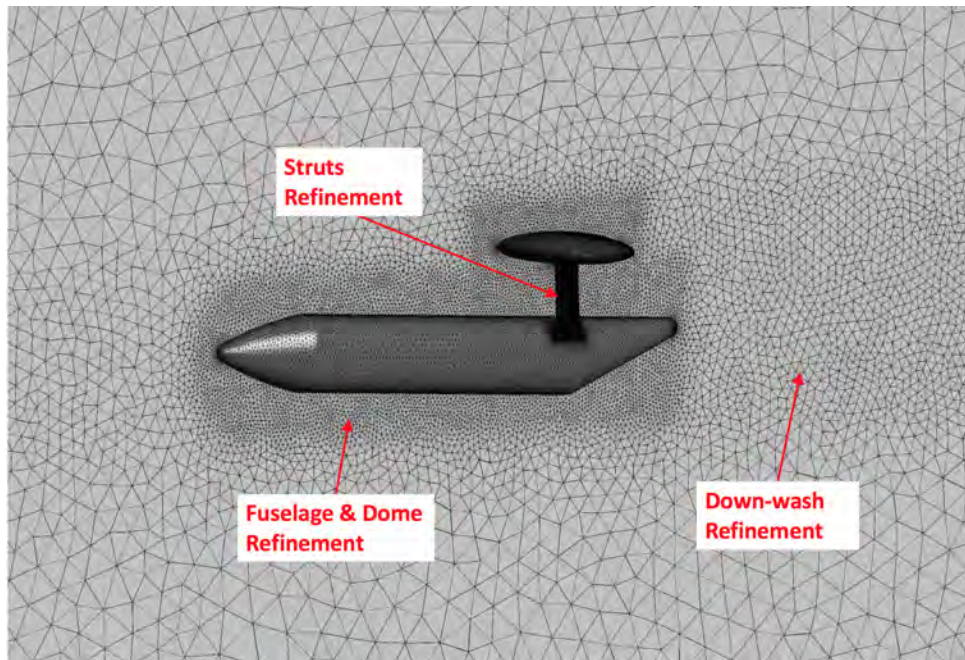
Figure 3.11: *Mesh grid*

For this simulation, the lift coefficient of the radar at an arbitrary incidence angle was chosen as the representative parameter to measure the solution accuracy. In Figure 3.12 five meshes of different grid sizing were tested to conclude that $1.5 \cdot 10^6$ nodes are satisfactory and any further refinement would lead to no improvement in the solution.
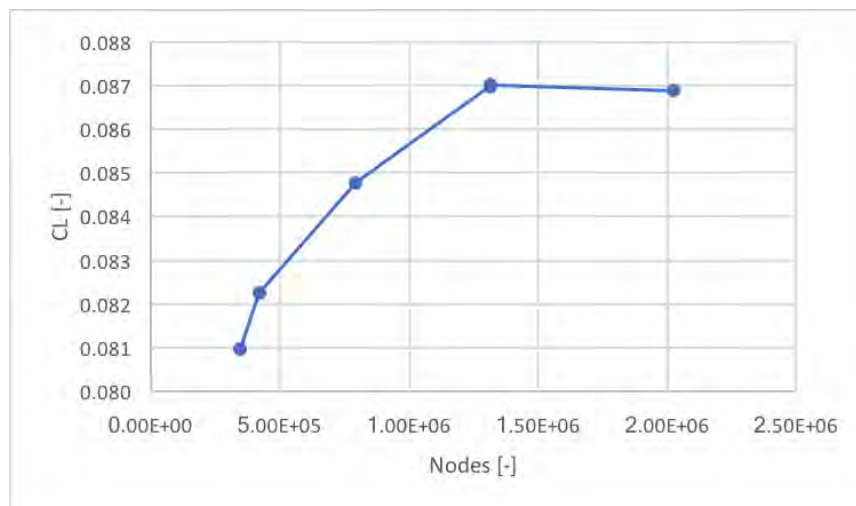
Figure 3.12: *Grid Independence Study*

3.4   Turbulence Model

> "Big whorls have little whorls,
> which feed on their velocity,
> and little whorls have lesser whorls
> and so on to viscosity"
>
> Lewis F. Richardson (1881-1953)

Turbulent flows are affected by the presence of walls, where viscosity dominates. In these near-wall regions, the presence of large gradients in the solution requires of a proper grid sizing if the nature of the boundary layer wants to be captured.

In CFD simulations, the wall non-dimensional distance y^+ is often used to analyse how coarse or fine a mesh is for a particular flow. This distance was introduced by Gerasimov in his seminar *Modeling Turbulent Flows using Fluent* from ANSYS [19] in 2006 and it helps to choose the most convenient near-wall treatment (wall functions or near-wall modeling) and turbulence model.

$$y^+ = \frac{U_\tau \cdot \Delta y_1}{\nu} \tag{3.1}$$

where ν is the air kinematic viscosity, U_τ the frictional velocity and Δy_1 the height of the grid cell.

3.4.1   Turbulent Wall Boundary Conditions

For a flat plate, it is generally accepted that the critical Reynolds number at which the flow starts the transition to turbulent is around $Re_{cr} \approx 5 \cdot 10^5$ and the flow is completely turbulent for $Re > 3 \cdot 10^6$, Incropera et al. [25, p. 361]. The flow studied in this experiment, $V_{air} = 68.05 \ m/s$, $rho_{air} = 1.225 \ kg/m^3$, $\mu_{air} = 1.8205 \cdot 10^{-5} \ kg/(m \cdot s)$ results in a $Re = 4.19 \cdot 10^7$ which lies in the turbulent region. As shown in Figure 3.13, a turbulent boundary layer is divided into three regions:

- Outer or defect region - Large scale turbulent eddy shear are dominant and the thickness of the layer depends on the Reynolds Number, typically for $y^+ > 500$

- Log-law layer - velocity shows a logarithmic profile, $30 < y^+ < 500$

- Inner region - where viscosity predominates. It can be subdivided into:

    - Buffer layer - transition between viscous and inertial layers, $5 < y^+ < 30$

    - Linear Sublayer - thin layer where viscosity dominates and it can be assumed that velocity follows a linear profile ($y^+ < 30$).
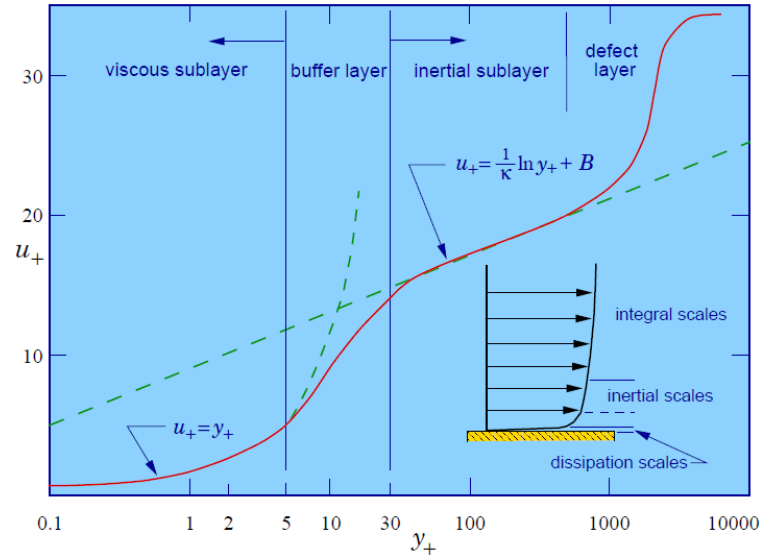
Figure 3.13: *Turbulent boundary layer regions [50]*

This is called the 'Law of the Wall' and was first established by Theodore von Kármán in 1931 [28] as a good approximation of the fluid velocity profile under the influence of viscosity in a near-wall area.

Close to the wall, the turbulent shear stress is negligible and viscous shear is responsible for damping the tangential velocity. Thus the shear of the fluid is defined as almost constant and equal to the wall shear stress such as,

$$\tau(y) = \mu \frac{\partial u}{\partial y} \simeq \tau_w \tag{3.2}$$

where, τ is the fluid shear stress, τ_w is the wall shear and μ is the fluid dynamic viscosity

Applying boundary conditions and solving for the non-dimensional tangential velocity in Equation (3.2), a linear relation with the non-dimensional wall distance is obtained. This is the linear sub-layer or the laminar sub-layer.

$$u^+ = y^+ \tag{3.3}$$

As we move further from the wall, outside the viscosity region ($30 < y^+ < 500$), both turbulent and viscous terms effects are equally significant and the shear is assumed to change gradually with the wall distance. Then, the non-dimensional velocity, u^+, is logarithmically related to y^+. This is the log-law.

$$u^+ = \frac{1}{k} \ln(y^+) + B \tag{3.4}$$

where, k is the Von-Karman constant, $k = 0.42$, and B is an empirical constant which depends on the roughness of the wall.

In-between these two regions, it is found the buffer layer ($5 < y^+ < 30$). Here, neither law holds for describing the velocity profile, which shows a steep gradient, especially at the intercept of the linear and logarithmic profiles, $y^+ \simeq 11.225$. Therefore, an approximation to one of each of the relations given in Equations (3.3) - (3.4) is usually made in these region.

3.4.2   The SST Model

Most CFD software includes different turbulence models to overcome the limitations of computers to resolve turbulences numerically. The CFD methods make use of turbulence model equations to estimate the turbulent stresses in order to solve the Reynolds-Averaged Navier-Stokes equations.

The turbulence model used for setting this simulation is the Shear-Stress Transport (SST) of Menter, [33, 34]. This model combines the advantages k-e and the k-ω to ensure a closed approach formulation of the flow characteristics.

The Wilcox k-ω [54] is a very robust model and predicts accurately the turbulent length scales near the wall-surface for adverse pressure gradients. Besides, it gets a simple formulation at low-Reynolds Numbers what makes it very reliable for viscosity-affected areas. However, as discussed in detail by Menter in [32], it is constrained by the strong sensitivity of the solution to the inlet free stream values of the turbulent frequency ω outside the boundary layer.

The k-ϵ model [27], on the other hand, has restrictions when applied to a near-wall region because it tends to over-predict the turbulent length scale. Therefore, in presence of adverse pressure gradients, it leads to higher wall shear stresses and a late prediction of the onset of the flow separation.

The limitations of both models are overcome by the SST model. For this, the k-ω is used in near-wall regions all the way down to the viscous sub-layer and switches to the k-ϵ model in the free shear region of the bulk flow to avoid the sensitivity problems described previously. This change is guided by means of a blending function, see [4] for detailed information.

3.4.3   Wall functions & First cell height

The near-wall representation of the flow is key to success predicting the numerical solution in a CFD simulation. The formulation in regions close to the wall determines the accuracy of the shear stress and heat transfer. Two approaches were considered for this purpose:

- Wall functions, Figure 3.14 (Left).
- Low-Reynolds number method or Zonal model approach, Figure 3.14 (Right).

The low-Reynolds method, as seen in Figure 3.14, involves a complete solving of the the laminar viscous sub-layer by placing a sufficient number of fine grid nodes between the wall and the near-wall region, where the logarithmic law applies. This method is not trivial as the user needs to take care of the grid-spacing, besides further refining does not necessarily imply better results. Hence, it is time consuming, computationally expensive and it can lead to poor results.

On the other hand, the wall function approach in the SST turbulence model uses empirical formulae to solve the flow conditions in the viscous sub-layer.
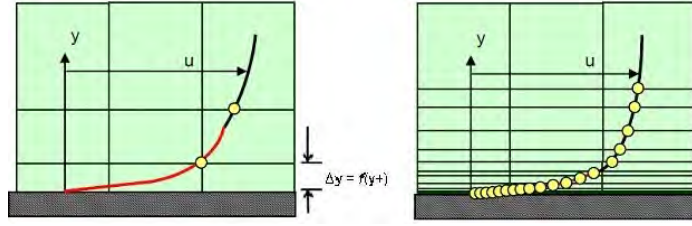
Figure 3.14: *Differences in the wall treatment of the viscous sub-layer [30]*

The k-ω based models takes advantage of the fact that an analytical expression is known for the turbulent frequency ω [54], and therefore the laminar sub-layer region is automatically bridged connecting the wall with the turbulent region, where mean velocity follows a logarithmic scale, as shown in Figure 3.14. A blending function is in charge of the switch between the log-law region and the viscous sub-layer based on the grid density making these model robust and simple.

In this simulation, the high Reynolds number implies a little gain if the viscous layer is solved in detail by the low-Reynolds method, which will be computationally more expensive, therefore, the wall function is preferred.

With this approach, it is important to ensure that the placement of the first cell of the grid lies inside the logarithmic layer at a wall distance $30 < y^+ < 500$, in order for the function to resolve the pressure drop and flow characteristics.

The height of the first cell is a function of the non-dimensional distance y^+ and it is computed based on its definition in Equation (3.1).

The y^+ distance and the air properties are imposed, and the frictional velocity U_τ is obtained as,

$$U_\tau = \sqrt{\frac{\tau_w}{\rho}} \tag{3.5}$$

where τ_w is the wall shear stress.

The wall shear τ_w is proportional to the dynamic pressure of the air and the skin-frictional coefficient C_f, Equation (3.6). As the Reynolds number is $4.19 \cdot 10^7$, thus within the turbulent boundary layer region and the body is a oblate spheroid with a thin aspect ratio $\lambda = 0.2$, C_f uses the empirical estimation for a thin plate in a turbulent external flow defined in Equation (3.7).

$$\tau_w = \frac{1}{2} \cdot C_f \cdot \rho \cdot U_\infty^2 \tag{3.6}$$

$$C_f = 0.058 \cdot Re_x^{-1/5} \tag{3.7}$$

Hence, combining Equations (3.1) - (3.7), the first cell height is obtained for a given target $y^+ = 200$, fluid properties and the characteristic length of the body such as,

$$\Delta y_1 = \frac{y^+ \cdot \nu}{\sqrt{0.029U_\infty}} Re_x^{1/10} \tag{3.8}$$
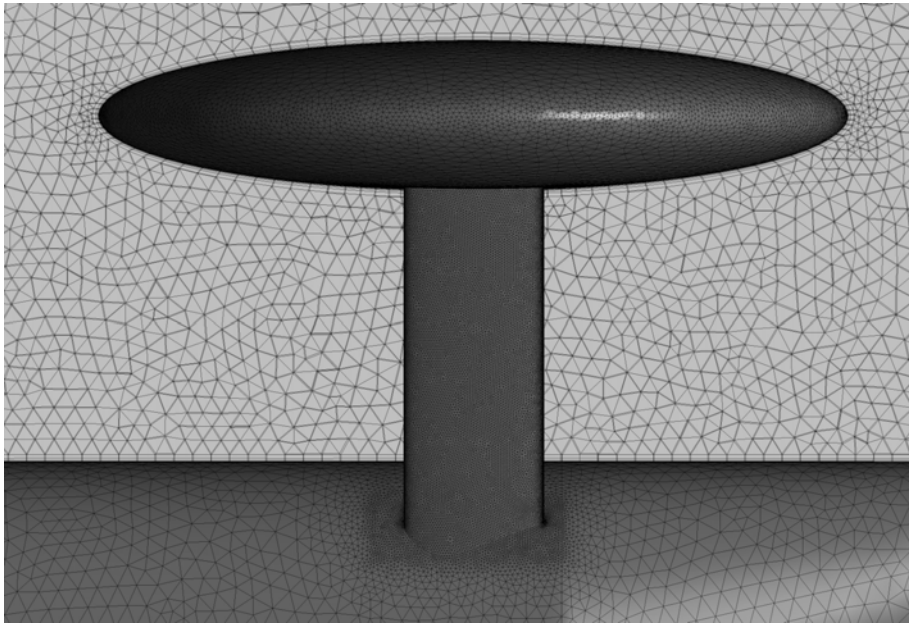
Figure 3.15: *Detailed view of the mesh*

Furthermore, the minimum required thickness of the refined structured inflation layer can be estimated through an empirical relation in Equation (3.9) for the boundary layer maximum thickness $\delta_m ax$ for a flat plate in a turbulent region as,

$$\delta_{max} = 0.373 \cdot \left(\frac{\nu}{U_\infty}\right)^{1/5} \cdot L^{4/5} \tag{3.9}$$

where L is the characteristic length and μ is the dynamic viscosity.

3.5   Pressure coefficient distributions

The distribution pressure coefficient C_p around the dome are depicted in Figure 3.17 for angles of attack ranging from 0 to 15°. The pictures show the low-pressure region originated below the dome when the air goes through between the struts. It is because of this *'tunnel effect'* that the lift force of the dome is found to be negative for most of the positive angles of attack.
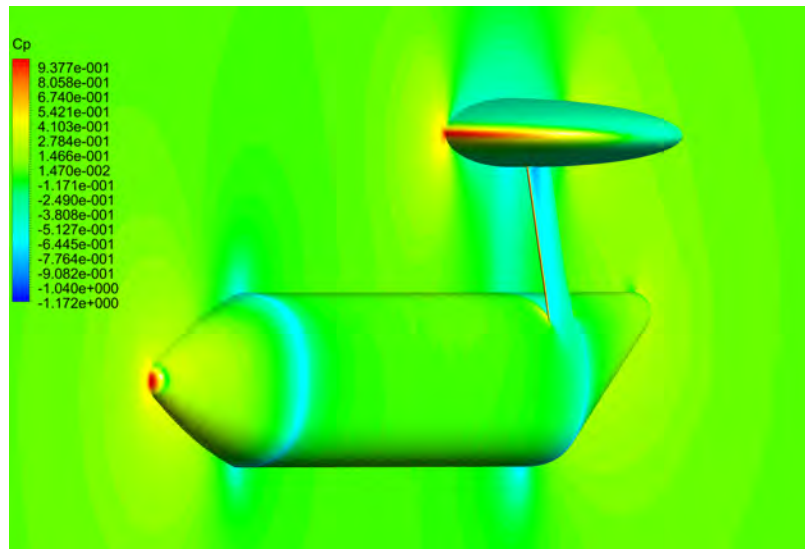
Figure 3.16: *Aircraft pressure coefficient distribution at the plane of symmetry*

$\alpha = 0^o$

$\alpha = 5^o$

$\alpha = 10^o$

$\alpha = 15^o$
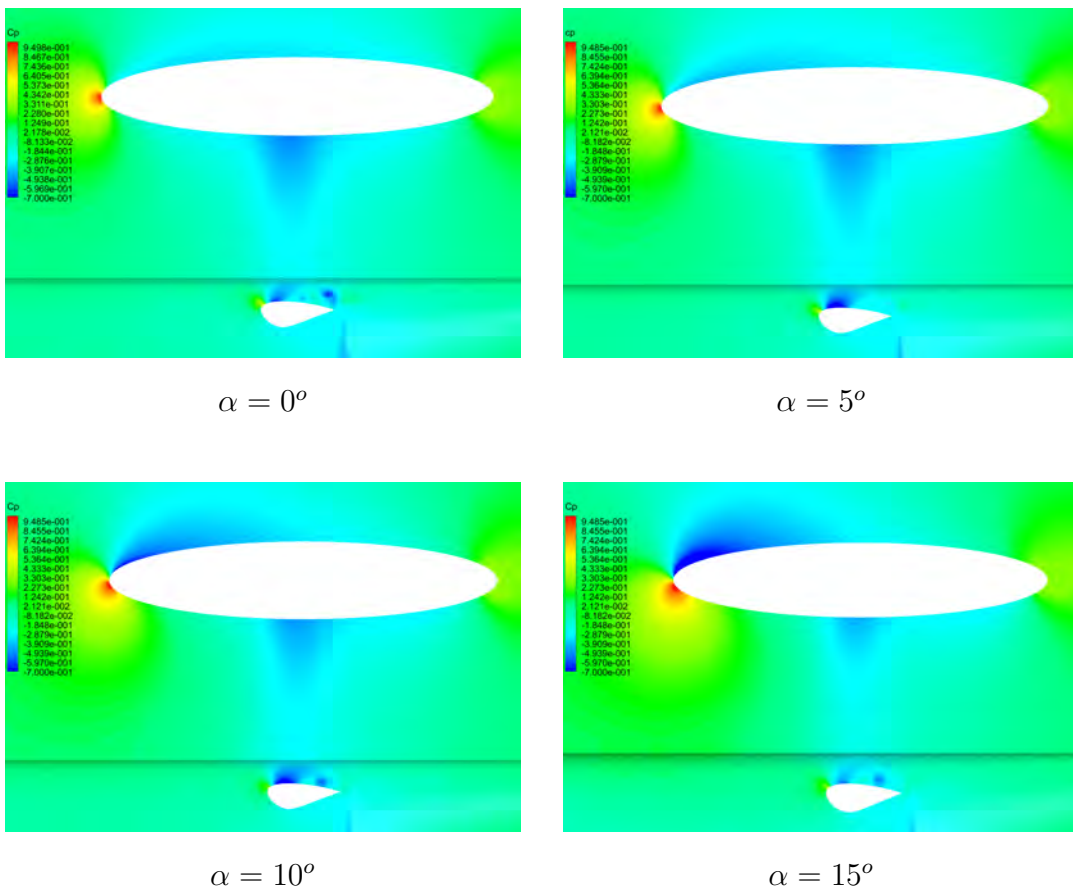
Figure 3.17: Dome pressure coefficient distribution at the plane of symmetry

Furthermore, Figure 3.18 shows the surface streamlines at the rear part of dome and the struts.
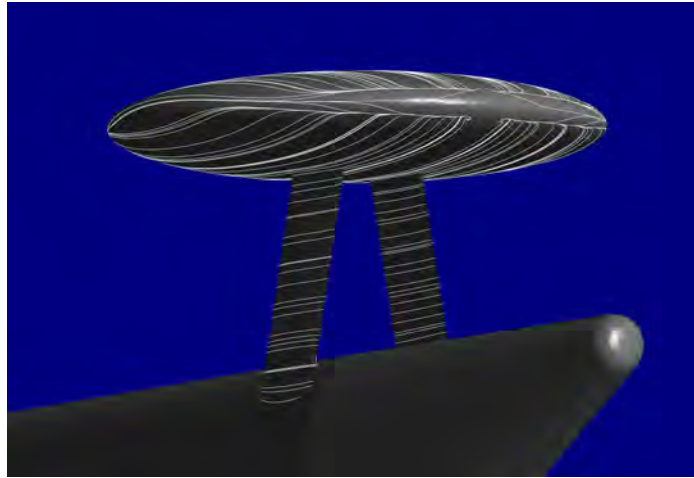
Figure 3.18: *Surface streamlines at the rear part radar*

3.6   Summary Computational Parameters

A summary of the computational parameters for the experiment are itemized in Table 3.1.

Table 3.1: Computational Parameters

Parameters	Setting
Mesh Type	Unstructured with local refinements
Number of elements	$\sim$ 6 millions
Number of nodes	$\sim$ 1.5 millions
y^+	200 with 7 layers in the boundary layer
Turbulence Model	Shear Stress Transport
Inlet turbulent intensity	5%
Wall Modelling	Automatic Wall Function
Advection Scheme	High Resolution
Timescale Control	Auto Timescale
Convergence Criteria	RMS residual $< 10^{-5}$
Computing	ANSYS CFX 16.2 with Double Precision
Run Type	Local Parallel processing (8 cores) RAM
Processor	Intel Core i7 with 16GB RAM
Simulation Time	5 - 6 hours

Chapter 4

Aerodynamic & Inertial AWACS Models

"Essentially, all models are wrong, but some are useful"

George E. P. Box (1919-2003)

4.1   Dome Reference Frame

The aerodynamic and inertial models compute the loads in a reference frame whose origin is located at the dome geometric centre as shown in Figure 4.1.
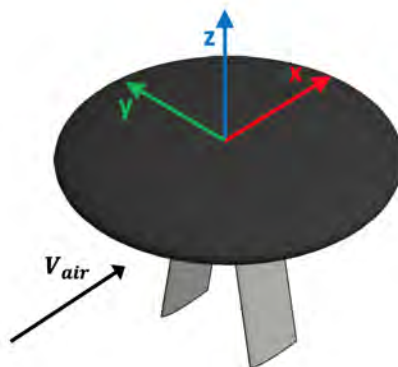
Figure 4.1: *Dome Reference Frame*

4.2   Aerodynamic Model

4.2.1   Regression Analysis: Principles of the Least Square Method

According to Alan O. Sykes from The University of Chicago,*"the regression analysis is a statistical tool for the investigation of relationships between variables"* [42].

Among the different techniques to identify model parameters from measured data we will focus on the linear least square regression, which is by far the most used modelling method due to the direct approach and relative simplicity. It works on the principle of finding the best-fitting curve for the measured data that minimizes the sum of the squared of the offsets ("residuals") of the points from the curve.

Given a model of data measurements, we wish to identify a set of n nominally constant parameters a_i which relate a set of state variables $X_{i,j}$ to measurements representing the output y of the process. In this formulation, the output vector y is measured with an error which is collected into a term ϵ. The regression can be expressed in a general form as,

$$y(k) = \sum_{i=1}^{n} X_i(k)a_i + \epsilon(k) \tag{4.1}$$

where m measurements sets are available in each state and output vector, x and y. Therefore,

$$a = \begin{pmatrix} a_1 \\ a_2 \\ \vdots \\ a_n \end{pmatrix}; \qquad X = \begin{pmatrix} x_{1,1} & x_{1,2} & \cdots & x_{1,n} \\ x_{2,1} & x_{2,2} & \cdots & x_{2,n} \\ \vdots & \vdots & \ddots & \vdots \\ x_{m,1} & x_{m,2} & \cdots & x_{m,n} \end{pmatrix}; \qquad y = \begin{pmatrix} y_1 \\ y_2 \\ \vdots \\ y_m \end{pmatrix}$$

The regression process results in an estimated $\hat{a}$ of the parameter vector a. Given this, the residuals may be defined as,

$$\epsilon = y - \hat{y} = y - X\hat{a} \tag{4.2}$$

where the estimated $\hat{a}$ minimises the sum of the squares of the residuals.

$$\min \sum_{k=1}^{m} \epsilon_k^2 = \min(\epsilon^T \cdot \epsilon) = \\ = \min\left((y - X\hat{a})^T \cdot (y - X\hat{a})\right) \tag{4.3}$$

For the minimum to exist, ϵ must satisfy that,

$$\frac{\partial}{\partial \hat{a}}(\epsilon^T \cdot \epsilon) = 2\frac{\partial \epsilon^T}{\partial \hat{a}}\epsilon = 0 \tag{4.4}$$

31

And substituting Equation (4.2) results in the general least square minimum solution,

$$-2X^T(y - X\hat{a}) = 0 \tag{4.5}$$

$$\hat{a} = (X^T X)^{-1} X^T y \tag{4.6}$$

4.2.2 Model

The CFD simulation is run at several incidence and sideslip angles and the loads are recorded. Subsequently, the least square regression is applied.

As a first approximation, the aerodynamic loads were modelled as linear functions of the incidence angle α and the sideslip angle β. However, further analysis determined that the force in the x-direction fit better a quadratic model. This statement is in close agreement with a polar drag model in which the drag force increases as the square of the lift, whereas the lift is assumed to increase linearly with the angle of attack prior to the stall.

$$C_D = C_{D_0} + kC_L^2 \tag{4.7}$$

$$C_L = C_{L_0} + C_{L_\alpha}\alpha \tag{4.8}$$

Therefore, a quadratic model is used for the non-dimensional force in the X direction and a linear model for the ones in the Y and Z directions as described in Equations (4.9) - (4.10).

$$C_x = \frac{F_x}{Q \cdot S_d} = C_{x_0} + \frac{\partial C_x}{\partial \alpha} \cdot \alpha + \frac{\partial C_x}{\partial \beta} \cdot \beta + \frac{\partial C_x}{\partial \alpha^2} \cdot \alpha^2 + \frac{\partial C_j}{\partial \beta^2} \cdot \beta^2 \tag{4.9}$$

$$C_i = \frac{F_i}{Q \cdot S_d} = C_{i_0} + \frac{\partial C_i}{\partial \alpha} \cdot \alpha + \frac{\partial C_i}{\partial \beta} \cdot \beta \qquad for \qquad i = y, z \tag{4.10}$$

where Q is the dynamic pressure $Q = \frac{1}{2}\rho V^2$ and Sd is the planform surface of the dome.

Similarly, the linear model for the non-dimensional moments around the three reference axis is defined in Equation (4.11) as,

$$C_j = \frac{M_j}{Q \cdot S_d \cdot D} = C_{j_0} + \frac{\partial C_j}{\partial \alpha} \cdot \alpha + \frac{\partial C_j}{\partial \beta} \cdot \beta \qquad for \qquad j = l, m, n \tag{4.11}$$

where D is the diameter of the dome.

4.2.3 Aerodynamic Coefficients
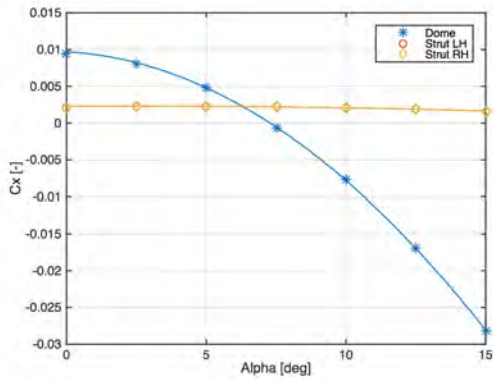
Figure 4.2: *X-Force coefficient versus angle of attack*
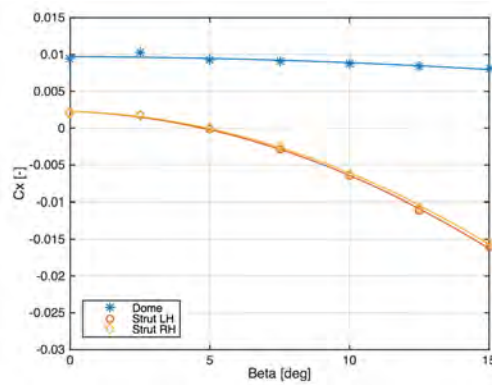
Figure 4.3: *X-Force coefficient versus sideslip angle*
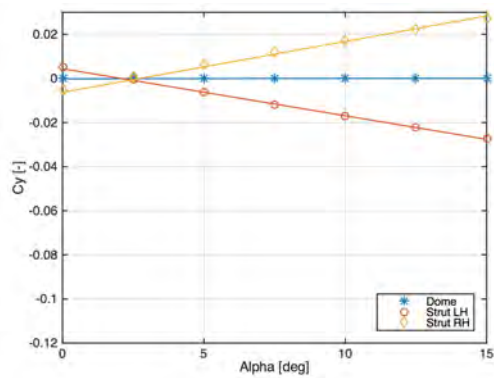
Figure 4.4: *Y-Force coefficient versus angle of attack*
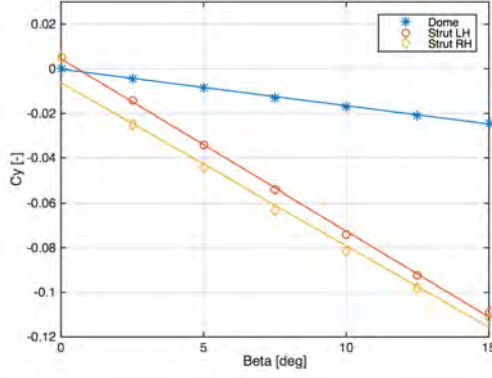
Figure 4.5: *Y-Force coefficient versus sideslip angle*
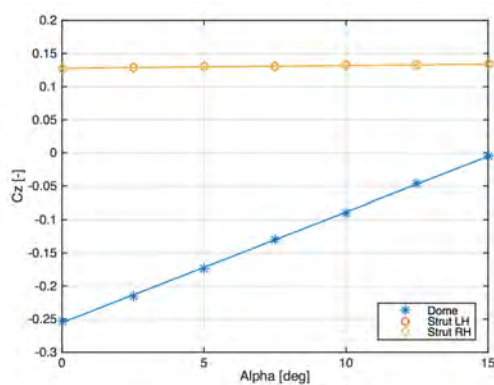
Figure 4.6: *Z-Force coefficient versus angle of attack*
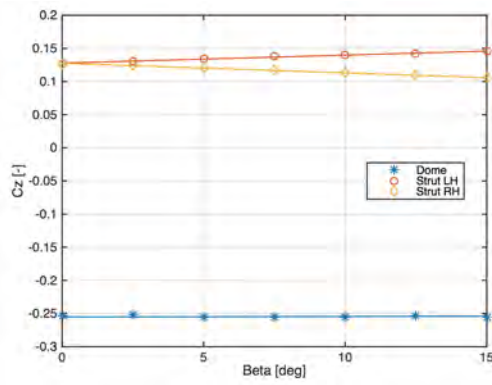
Figure 4.7: *Z-Force coefficient versus sideslip angle*

Figures 4.2 - 4.7: Forces at the three reference axis
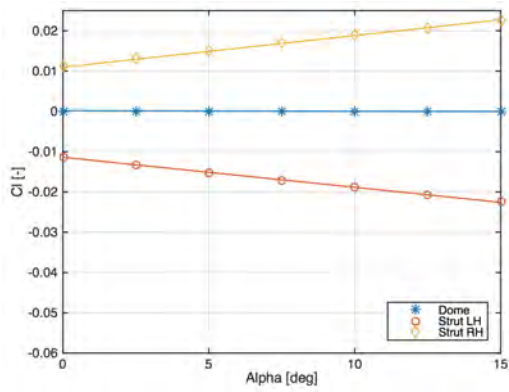
Figure 4.8: *Roll moment coefficient versus angle of attack*
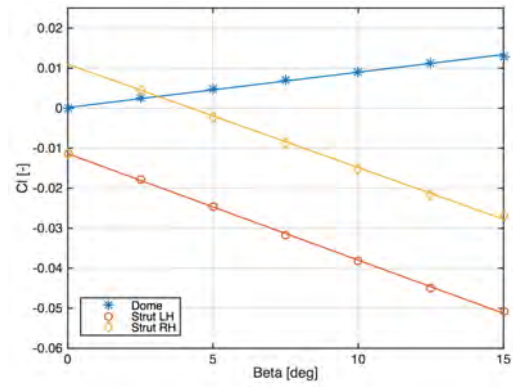
Figure 4.9: *Roll moment coefficient versus sideslip angle*
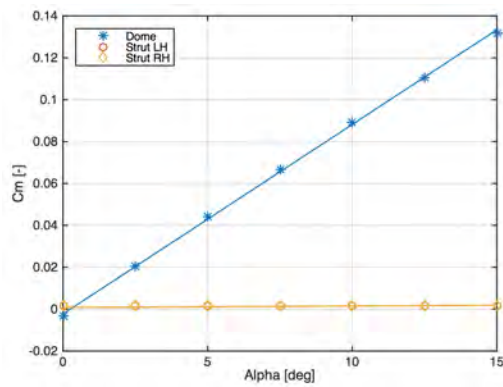
Figure 4.10: *Pitch moment coefficient versus angle of attack*
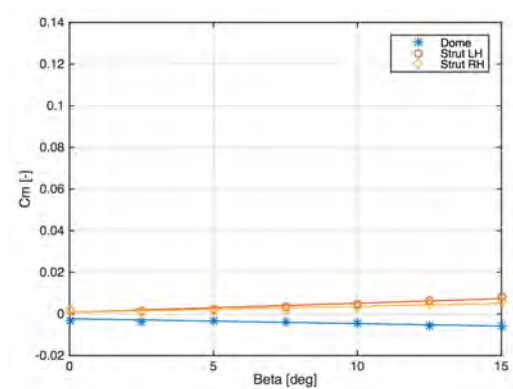
Figure 4.11: *Pitch moment coefficient versus sideslip angle*
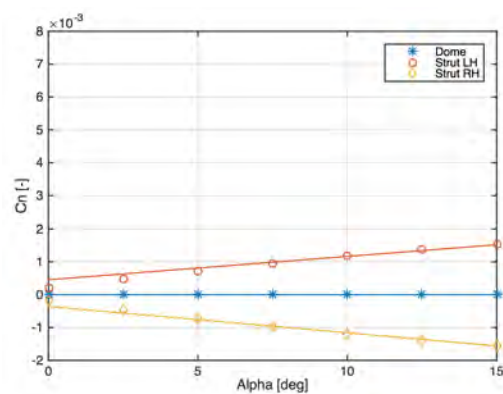
Figure 4.12: *Yaw moment coefficient versus angle of attack*
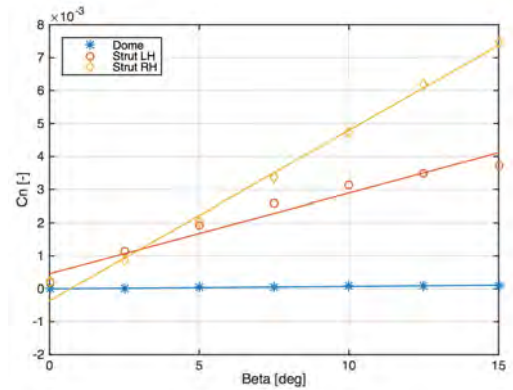
Figure 4.13: *Yaw moment coefficient versus sideslip angle*

Figures 4.8 - 4.13: Moments around the three reference axis

Table 4.1: Aerodynamic force coefficients with the angle of attack

	C_{i0} [-]			$\partial C_i / \partial \alpha$ [rad^{-1}]			$\partial C_i / \partial \alpha^2$ [rad^{-2}]		
	Dome	**Strut LH**	**Strut RH**	**Dome**	**Strut LH**	**Strut RH**	**Dome**	**Strut LH**	**Strut RH**
Fx	0.0097	0.0023	0.0023	-0.0122	0.0013	0.0011	-0.5049	-0.0141	-0.0136
Fy	-0.0002	0.0044	-0.0063	0.0009	-0.1224	0.1324	0.0000	0.0000	0.0000
Fz	-0.2552	0.1278	0.1275	0.9546	0.0223	0.0239	0.0000	0.0000	0.0000

Table 4.2: Aerodynamic force coefficients with the sideslip angle

	C_{i0} [-]			$\partial C_i / \partial \beta$ [rad^{-1}]			$\partial C_i / \partial \beta^2$ [rad^{-2}]		
	Dome	**Strut LH**	**Strut RH**	**Dome**	**Strut LH**	**Strut RH**	**Dome**	**Strut LH**	**Strut RH**
Fx	0.0097	0.0023	0.0023	-0.0007	-0.0078	-0.0063	-0.0228	-0.2409	-0.2385
Fy	-0.0002	0.0044	-0.0063	-0.0939	-0.4411	-0.4175	0.0000	0.0000	0.0000
Fz	-0.2552	0.1278	0.1275	0.0044	0.0690	-0.0830	0.0000	0.0000	0.0000

Table 4.3: Aerodynamic moment coefficients with the angle of attack

	C_{i0} [-]			$\partial C_i/\partial \alpha$ [rad^{-1}]			$\partial C_i/\partial \alpha^2$ [rad^{-2}]		
	Dome	**Strut LH**	**Strut RH**	**Dome**	**Strut LH**	**Strut RH**	**Dome**	**Strut LH**	**Strut RH**
Mx	0.0002	-0.0114	0.0110	-0.0008	-0.0427	0.0450	0.0000	0.0000	0.0000
My	-0.0023	0.0008	0.0008	0.5184	0.0041	0.0042	0.0000	0.0000	0.0000
Mz	0.0000	0.0005	-0.0004	0.0000	0.0041	-0.0046	0.0000	0.0000	0.0000

Table 4.4: Aerodynamic moment coefficients with the sideslip angle

	C_{i0} [-]			$\partial C_i/\partial \beta$ [rad^{-1}]			$\partial C_i/\partial \beta^2$ [rad^{-2}]		
	Dome	**Strut LH**	**Strut RH**	**Dome**	**Strut LH**	**Strut RH**	**Dome**	**Strut LH**	**Strut RH**
Mx	0.0002	-0.0114	0.0110	0.0505	-0.1523	-0.1479	0.0000	0.0000	0.0000
My	-0.0023	0.0008	0.0008	-0.0134	0.0249	0.0165	0.0000	0.0000	0.0000
Mz	0.0000	0.0005	-0.0004	0.0004	0.0140	0.0295	0.0000	0.0000	0.0000

4.3   Inertial Model

The inertial data refers to the mass, the moment of inertia tensor and the gravity centre location of the model. A preliminary estimation of these values serve to compute the inertial loads transmitted to the fuselage.

Regarding current industrial practices during the conceptual phases of a project, the engineers need to estimate the mass density and dimensions of the different systems fitted inside the radar. The estimation for the different elements are based on the experience gathered on system integration as well as the requirements imposed by the technical specifications of the aircraft, 'Top Level Aircraft Requirements' (TLAR) and the contract specifications agreed with the client, Certification Review Item (CRI). Subsequently, the Mass Properties Department incorporates the information into a computer model which calculates the inertial data accurately, especially the inertia tensor. This is important because the use of the software permits to reflect instantaneous updates in the design.

In this thesis, the radar is modelled in a CAD software. Based on data from the existing AWACS E3-Sentry in [36], the nominal mass of the dome and struts assembly is established at 13,000 lbs or 5896.5 kg. The main assumption in this model is that the mass is distributed isotropically according to the volume, which allows to estimate the average mass density and subsequently the mass of the dome and each strut separately.

4.3.1   Inertial data

The mass and gravity centre of the dome and each strut with respect to the radar coordinate system are:

Table 4.5: Mass and gravity centre location of the radar assembly

	Mass [kg]	X-CG [m]	Y-CG [m]	Z-CG [m]
Dome	5739.95	0	0	0
Left Strut	78.29	-0.14	-1.24	-3.11
Right Strut	78.29	-0.14	1.24	-3.11
Global	5896.52	$-4 \cdot 10^{-3}$	0	$-8 \cdot 10^{-2}$

The global inertia tensor for the assembly referenced to the radar reference system.:

$$I_{global} = \begin{pmatrix} I_{xx} & I_{xy} & I_{xz} \\ I_{xy} & I_{yy} & I_{yz} \\ I_{xz} & I_{yz} & I_{zz} \end{pmatrix} = \begin{pmatrix} 26999.77 & 0 & -65.82 \\ 0 & 26778.69 & 0 \\ -65.82 & 0 & 48270.04 \end{pmatrix}$$

Where,

$$I_{xx} = \int (y^2 + z^2)dm \qquad\qquad I_{xy} = -\int (xy)dm$$

$$I_{yy} = \int (x^2 + z^2)dm \qquad\qquad I_{yz} = -\int (yz)dm$$

$$I_{zz} = \int (x^2 + y^2)dm \qquad\qquad I_{xz} = -\int (xz)dm$$

And the inertia tensors for each of the three elements of the radar: dome, left strut and right strut, are:

$$I_{dome} = \begin{pmatrix} 24956.50 & 0 & 0 \\ 0 & 24956.50 & 0 \\ 0 & 0 & 47993.28 \end{pmatrix}$$

$$I_{Left-St} = \begin{pmatrix} 1021.63 & -13.08 & -32.91 \\ -13.08 & 911.09 & -326.14 \\ -32.91 & -326.14 & 138.38 \end{pmatrix}$$

$$I_{Right-St} = \begin{pmatrix} 1021.63 & 13.08 & -32.91 \\ 13.08 & 911.09 & 326.14 \\ -32.91 & 326.14 & 138.38 \end{pmatrix}$$

4.3.2   Equations of inertial forces and moments

The inertial loads retain the inertia land gravitational effects for given flight conditions. The equation for the inertial forces are:

$$F_{x_i} = -m \cdot (gN_x + z\dot{q} - y\dot{r} - x(q^2 + r^2) + zpr + ypq) \tag{4.12}$$
$$F_{y_i} = -m \cdot (gN_y + x\dot{r} - z\dot{p} - y(p^2 + r^2) + xpq + zqr) \tag{4.13}$$
$$F_{z_i} = -m \cdot (gN_z - x\dot{q} + y\dot{p} - z(q^2 + p^2) + xpr + yqr) \tag{4.14}$$

where $x = x_{cg_i} - x_{ref}$; $y = y_{cg_i} - y_{ref}$; $z = z_{cg_i} - z_{ref}$

The load factor N_x, N_y, N_z are defined as:

$$N_x = -(F_{Ax} + F_{Tx})/mg = -\sin\theta - (\dot{u} - rv + qw)/g \tag{4.15}$$
$$N_y = -(F_{Ay} + F_{Ty})/mg = -\cos\theta\sin\phi - (\dot{v} - pw + ru)/g \tag{4.16}$$
$$N_z = -(F_{Az} + F_{Tz})/mg = -\cos\theta\cos\phi - (\dot{w} - qu + pv)/g \tag{4.17}$$

The equations for the inertial moments are:

$$M_{x_i} = I_{xx}\dot{p} - I_{xy}\dot{q} - I_{xz}\dot{r} + (I_{zz} - I_{yy})qr + I_{yz}(r^2 - q^2) + I_{xy}pr - I_{xz}pq \tag{4.18}$$
$$M_{y_i} = I_{yy}\dot{q} - I_{xy}\dot{p} - I_{yz}\dot{r} + (I_{xx} - I_{zz})qr + I_{xz}(p^2 - r^2) + I_{yz}pq - I_{xy}qr \tag{4.19}$$
$$M_{z_i} = I_{zz}\dot{r} - I_{xz}\dot{p} - I_{yz}\dot{q} + (I_{yy} - I_{xx})pq + I_{xy}(q^2 - p^2) + I_{xz}qr - I_{yz}pr \tag{4.20}$$

Chapter 5

AWACS Static Loads

The impact of the radar loads in the configuration of a hypothetical aircraft is of significant order and a preliminary estimation will serve the stress engineers to start the design of the structure and to trigger the loops that will end with the final certificated model.

The incremental static loads at the rear fuselage come from the joined contribution of two types of forces and moments: aerodynamic and inertial. On one side, the aerodynamic loads arise due to the geometric shapes and flight conditions; whilst, the inertia loads mostly result from the dynamics of the manoeuvres performed by the aircraft. For this reason, a preliminary aerodynamic model was developed with the help of a CFD software in Section 4.2, and the inertial model was discussed in Section 4.3.

In general terms, the required changes to accommodate a system of such dimensions and mass will focus on the rear fuselage whose structural frames will need to be reinforced, while further impact on the horizontal and vertical tails is to be assessed. The flight control laws of the aircraft shall have to be revised but this aspect is out of the scope of this thesis.

Regarding loads' regulations, there are two organizations in charge of setting them: EASA[1] (European Aviation Safety Agency) and FAA[2] (Federal Aviation Administration). Both certification authorities, EASA and FAA, enforce the compliance of the specifications for Large Aeroplanes CS-25 and FAR-25. Specifically, Subpart C - 'Structure' - deals with loads, separating the flight loads from the ground ones. This project is focused on the impact of the flight loads derived from manoeuvres where no gust loads are examined.

---

[1]https://www.easa.europa.eu/
[2]https://www.faa.gov/

5.1 Flight Envelope

According to CS/FAR-25.333(a), the flight manoeuvring envelope defines the combination of load factors and airspeeds (V-N diagram) at which the strengths requirements must be met, see Figure 5.1. The load factor is the ratio of the aerodynamic forces to the weight of the aircraft. At low speeds, the envelope is constrained by the stalling conditions, which depend on the weight; and at high speeds, it is limited by the design speed as defined in CS/FAR-25.335.
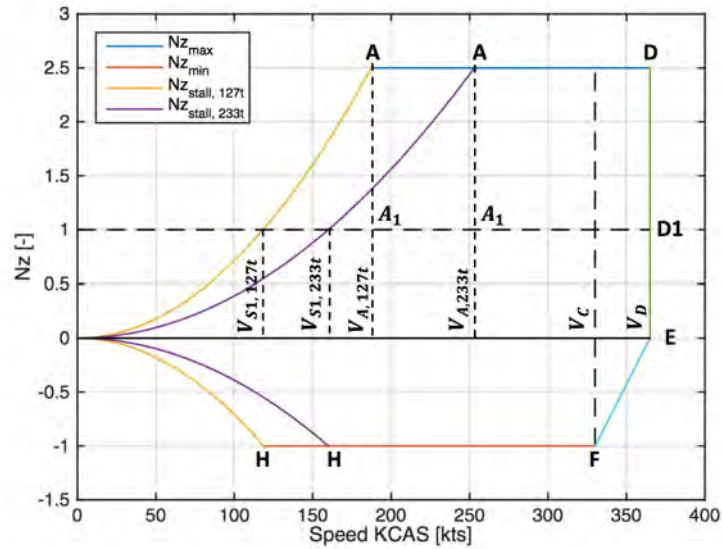
Figure 5.1: *Airbus A330-200 Flight Envelope*

The stalling speed is a function of the weight and the load factor. It is described by the vertical equilibrium equation and the definition of lift as follows:

$$V_s = \sqrt{\frac{W N_z}{\frac{1}{2}\rho S_{ref} C_{L_{max}}}} \tag{5.1}$$

where, S_{ref} is the wing surface, ρ is the air density and $C_{L_{max}}$ is the maximum lift coefficient.

In general, for civil and transport aircrafts the maximum load factor is established at 2.5 and the minimum one at -1. Particularly, the flight envelope for the reference aircraft Airbus A330-200 is specified in Table 5.1.

Table 5.1: Flight envelope data Airbus A330-200

Nz_{max}	2.5	V_C **[KEAS]**	330	M_C	0.86
Nz_{min}	-1	V_D **[KEAS]**	365	M_D	0.93
		Ceiling [ft]	41,000		

5.2   Flight Manoeuvres

The aircraft flight manoeuvring conditions applicable to the AWACS loads' calculation, without gust loads considerations, are defined in CS-25 and FAR-25 by the following regulations:

- 25.331 Symmetric manoeuvring conditions
- 25.349 Rolling conditions
- 25.351 Yaw manoeuvre conditions
- 25.367 Unsymmetrical loads due to engine failure conditions

5.2.1   Symmetric manoeuvring conditions

The symmetric manoeuvres described in CS/FAR-25.331 are comprised of two flight conditions: balanced N_z and pitching conditions.

5.2.1.1   Balanced N_z conditions

These are quasi-symmetrical flight condition with a specified vertical load factor N_z for which the force equations (4.12) - (4.20) are solved at zero linear and angular acceleration, as dictated by CS/FAR-25.331 (b). The manoeuvres correspond to a punctual instant, isolated and without time evolution. The aircraft is assumed to be at equilibrium. Design speeds and vertical load factor combinations are checked between points A to H of the flight envelope shown in Figure 5.1.

Two conditions must be considered:

1. Manoeuvres in the vertical plane
   These conditions include the pull-up and push-over.

2. Balanced steady turn
   Despite of having a large bank angle ϕ and possibly a significant yawing rate r, the balanced turn is analysed along with the manoeuvres in the vertical plane because, from the loads' standpoint, the lift distribution at the wings and HTP are comparable to those found in the pull-up conditions. This is a quasi-symmetric condition and in first approximation, both conditions are equivalent for the dome and struts when Equation (5.6) is applied.

(1) The balanced conditions in the vertical plane correspond to either the lowest point of a flight path in a pull-up manoeuvre, $N_z > 1$, or the uppermost point of the analogous push-over manoeuvre, $N_z < 1$, see Figure 5.2. They are symmetric in both cases and the pitch rate q is approximated by the Equation (5.2) at true airspeed. Roll and yaw rates are set to zero.

$$q \approx \frac{g}{V_{TAS}}(N_z - 1) \tag{5.2}$$
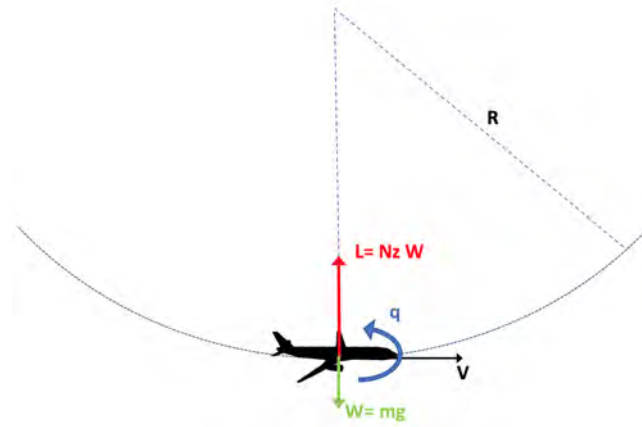
Figure 5.2: *Balance Nz manoeuvre in the vertical plane*

(2) The balanced turn is a steady condition at zero sideslip angle. In this case the pitch rate is approximated by Equation (5.3), where $N_z > 1$. The bank angle and yaw rate are estimated by Equations (5.4) - (5.5), which takes into account the turn to both sides, port and starboard.

$$q \approx \frac{g}{V_{TAS}}(N_z - \frac{1}{N_z}) \tag{5.3}$$

$$\phi \approx \arccos(1/N_z) \tag{5.4}$$

$$r \approx \pm q/\tan(\phi) \tag{5.5}$$

Furthermore, for both conditions the incidence angle may be estimated as a function of vertical load factor N_z from the definition of the lift coefficient as:

$$\alpha = \frac{W N_z}{Q S_{ref} C_{L_\alpha}} \tag{5.6}$$

The lift coefficient variation with alpha C_{L_α} of the aircraft is estimated from Equation 3.3.1 in Pester [37]:

$$C_{L_\alpha} = 2\pi \cdot \frac{AR_w}{AR_w + 2} \tag{5.7}$$

Where AR_w is the wing aspect ratio.

5.2.1.2 Manoeuvring pitching conditions

These are symmetrical flight conditions starting at steady position and null pitch rate. Any aircraft roll or yaw perturbations should be neglected or assumed zero. The conditions described in CS/FAR-25.331(c) request to analyse the maximum elevator displacement at V_A and several combinations of pitching rates in a range of airspeeds between V_A and V_D.

The pitching manoeuvring conditions tend to be critical for the horizontal tail-plane of the aircraft. However, it can be shown that they will not produce radar loads higher that the ones encounter by the 'Balanced N_z conditions' in Section 5.2.1.1, and therefore they can be ignored for the AWACS preliminary loads assessment.

Two conditions are described by the regulations:

1. Maximum pitch control displacement at V_A.
   The pitch control surface is suddenly deflected in order to get a extreme pitch-up, CS/FAR-25.331(c)(1). The aircraft is assumed to fly at point A_1 of its envelope as described in Figure 5.1. In aeroplanes with manual controls the elevator is moved to its maximum position, while in aircrafts with a flight control laws, a demand of maximum vertical load factor is produced and the control surface actuators act accordingly.

   The regulation states that there is no need to consider conditions subsequent to the instant at which maximum loads at the HTP are achieved or aircraft maximum vertical load factor is reached, whichever comes first. However, according to Lomax [31], the maximum loads at the tailplane are usually found at the very first instants of the manoeuvre, when the pitching acceleration $\dot{q}$ is maximum and N_z is closed to 1. As times goes by, the pitching rate increases the incidence angle α and the aerodynamic lift balances the inertial forces.

2. Checked manoeuvres between V_A and V_D.
   In aircraft with active control laws, the checked manoeuvres involve the periodic deflection of the elevator from steady flight conditions at any speed between V_A and V_D, CS/FAR-25.331(c)(2). The sinusoidal displacement must have a frequency equal to the undamped natural frequency of the aircraft's short-period rigid mode but never less than $\omega = \pi V/(2V_A)$ rad/s. The manoeuvre is analysed until the maximum design N_z is reached for pitch-up manoeuvres and $N_z = 0$ for pitch-down manoeuvres.

   In practice, the maximum vertical load factor is achieved in quasi-stationary conditions, and regarding radar loads, the manoeuvre is similar to the 'Balanced Nz conditions' in terms of incidence angle α and pitch rate q.

For the aforementioned reasons, the manoeuvring pitching conditions are not considered more critical than the 'Balanced Nz conditions' described in Section 5.2.1.1.

5.2.2 Lateral manoeuvring conditions

The lateral manoeuvring conditions are composed of three flight conditions: yaw manoeuvres, rolling conditions and engine failure conditions..

5.2.2.1 Yaw manoeuvres conditions

These conditions involve rudder displacement in sideslip and a yaw rate. For yawing manoeuvres, the regulations CS/FAR-25.351(a-d) establishes four critical instants to be analysed:

1. Sudden rudder deflection at $\beta = 0$
2. Maximum β-overshoot
3. Static equilibrium at maximum sideslip
4. Return of rudder control to neutral position

In the case of manual controls, the aircraft response to a rudder deflection is closed to a second order system according to the Dutch roll eigen-modes first approximation. However in the case of aircraft with flight control laws, the rudder deflection is affected by closed-loop gains in most of the lateral stability variables, including the yawing rate. Overall these gains effectively behaves as an artificial *yaw damper* counteracting the response of the Dutch roll, which this time resembles a first order system. The β-overshoot disappears. A comparison of the lateral response to rudder deflection of both system is shown in Figure 5.3.
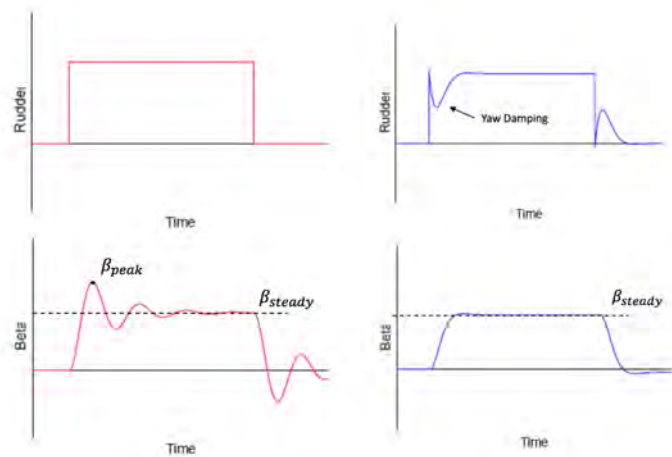
Figure 5.3: *Lateral response due to rudder deflection. (a) Left: Manual controls. (b) Right: Active flight control laws*

The four critical instants above mentioned are relevant for the loads concerning the vertical tail and the rudder. However, for the dome and struts in a fly-by-wire aircraft, as it is the one considered for this thesis, the critical conditions may be reduced to one: the static equilibrium at maximum sideslip angle $\beta = \beta_{steady}$. The aircraft is yawed to the static equilibrium

condition at maximum deflection of rudder. It is assumed a straight and steady sideslip flight with null angular rates. The rudder control is governed by the rudder travel limiter, as shown later on in Figure 5.7.

The airspeeds range for these conditions must be between the minimum control speed V_A and the diving speed V_D. Besides, the maximum sideslip angles considered are a function of the speed as shown in Figure 5.8.

5.2.2.2 Rolling conditions

This group of manoeuvres comprise aileron displacement and a roll rate. For aircraft with flight control laws, these conditions must be combined with a vertical load factor ranging from zero to two third of the maximum N_z. CS/FAR-25.349(a) establish three velocity conditions to be considered:

- Maximum aileron deflection at V_A, resulting in the maximum roll rate.

- At V_C, aileron displacement to produce a roll rate equal to the one at V_A.

- At V_D, aileron displacement to produce a roll rate equal to one third of the one at V_A.
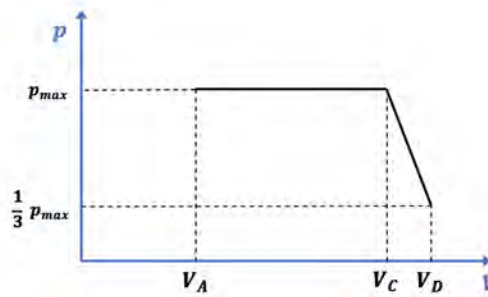
Figure 5.4: *Roll rate required by CS/FAR-25.349*

Nevertheless it can be shown that the sideslip angle induced by the maximum roll rate is lower than the maximum sideslip angle for the yawing manoeuvres. Consequently, in a first approximation, the AWACS lateral loads produced by the rolling manoeuvres are considered less critical than the ones described in Section 5.2.2.1.

As a result, the induced lateral speed due to a roll rate is expressed as $\Delta v = pH$ and the induced sideslip angle $\Delta\beta_{ind}$ is checked for $p = 30^o/s$, a height $H \approx 7$m. and the two air-speeds for which maximum roll rate is required by regulations as shown in Figure 5.4:

$$\Delta\beta_{ind} = \arcsin\left(\frac{\Delta v}{V}\right) \simeq \frac{\Delta v}{V} = \frac{pH}{V} = \begin{cases} 2.1^o & \text{for} \quad V_A = 100 \text{ m/s} \\ 1.23^o & \text{for} \quad V_C = 170 \text{ m/s} \end{cases} \quad (5.8)$$

Consequently, any of the $\Delta\beta_{ind}$ is an order of magnitude smaller than the sideslip transient angle achieved for a sudden rudder deflection at yawing manoeuvres, which is about $\beta \approx 18^o$ at V_A, see Figure 5.8. Therefore the lateral loads due to rolling conditions will not be critical for the radar.
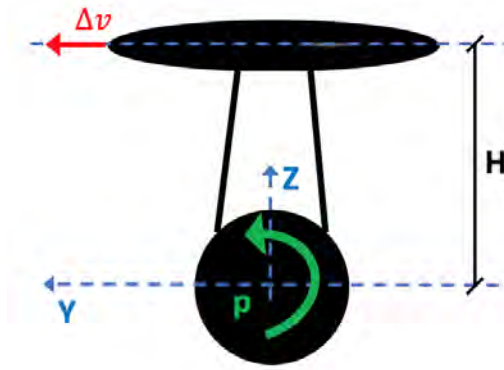
Figure 5.5: *Lateral velocity induced by the aircraft rolling rate*

Furthermore, in terms of vertical forces, the rolling conditions results in an upward centrifugal acceleration, which can be compared to the most negative vertical load factor shown in the flight envelope $N_z = -1$, Figure

The centrifugal acceleration is defined as:

$$\overrightarrow{a_{centr}} = \overrightarrow{\omega} \wedge (\overrightarrow{\omega} \wedge \overrightarrow{r}) \tag{5.9}$$

In particular, the absolute value of the vertical component is given by:

$$|\overrightarrow{a_z}| = p^2 H \tag{5.10}$$

Thus, the vertical load factor for the rolling condition is:

$$N_z = -\frac{|\overrightarrow{a_z}|}{g} = -\frac{p_{max}^2 H}{g} =$$
$$= -\frac{(30\frac{\pi}{180})^2 \cdot 7}{9.81} = -0.19 > -1 \tag{5.11}$$

Accordingly, the vertical factor due to the maximum roll rate is an order of magnitude lower than the one described by the balanced N_z conditions in Section 5.2.1.1.

5.2.2.3   Engine failure conditions

The conditions of one-engine-out conditions involved the unsymmetrical loads originated by a failed engine. The pilot correctiveness action is assumed to be initiated at the time of maximum yawing velocity but not earlier than 2 seconds, CS/FAR-25.367 (b). Thrust decay of the engine is supposed to occur instantaneously, which is a conservative assumption as opposed to any exponential decay function of time.

Regarding loads, two instants should be considered:

1. The failure transient state at maximum yawing velocity and no rudder correction implemented.
2. The engine failure steady state flight with the required rudder deflection at minimum control speed as defined in CS/FAR-25.149.

In general, condition (1) is meant to produce higher lateral loads than (2). The reason is that once the pilot correctiveness actions are implemented, mainly a rudder deflection, the aircraft must fly closed to zero sideslip angle as mandated by handling qualities specified in CS/FAR 25.149. Therefore, condition (2) is only a concern for the VTP and rudder but not for the AWACS radar.
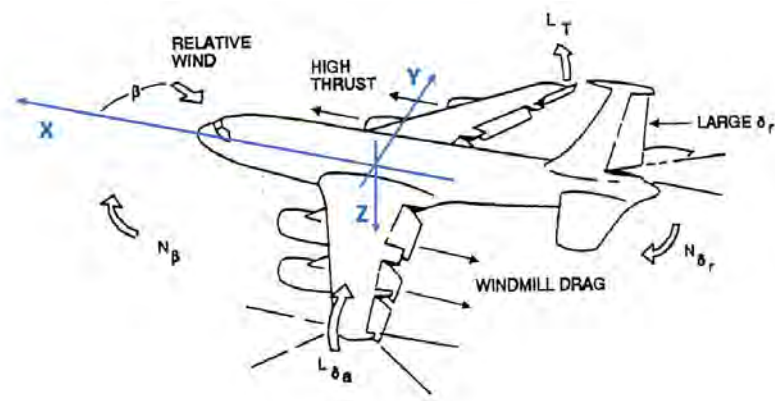
Figure 5.6: *Forces and moments in an engine-out failure [49]*

5.3   Directional Balance Analysis

The conclusion extracted from the previous section is that there are two flight conditions that might result critical for the lateral AWACS loads:

1. The yawing manoeuvres, CS/FAR-25.351.
2. The engine failure transient state, CS/FAR-25.367.

Here-onwards it is proven that condition (1) results in higher sideslip angles, and consequently produces the most critical lateral aerodynamics loads.

For the purpose of the analysis of the engine failure conditions, a thrust and wind-milling drag models are provided.

5.3.1   Engine thrust model

The maximum engine thrust available is dependent upon three parameters:

a Flight speed

b Flight altitude

c Engine operating conditions

According to Howe [23, p. 65-67], the thrust can be modelled as:

$$T_{avail} = \tau \cdot T_0 \tag{5.12}$$

where T_0 is the datum sea level static dry thrust and τ is the dependent factor.

The τ factor for a subsonic speed range $0.4 < M < 0.9$, and a typical turbofan bypass ratio $R = 5$ is defined as:

$$\tau = [0.88 - 0.016R - 0.3M]\sigma^{0.7} \tag{5.13}$$

where σ is the relative air density ratio.

5.3.2   Wind-milling drag model

The wind-milling drag is the opposing longitudinal force originated by the inoperative engine. This is estimated by Equation (5.14) using a method described in Torenbeek [45, appx. G-8] for turbofan engines.

$$C_{D_{mill}} = \frac{0.0785 \cdot d_i^2 + \frac{2}{1+0.16M^2}\frac{\pi}{4}d_i^2\frac{V_n}{V}\left(1 - \frac{V_n}{V}\right)}{S_{ref}} \tag{5.14}$$

where,

- $d_i \equiv$ engine inlet diameter (≈ 3 m.)
- $V_n \equiv$ is the nozzle exit velocity
- $V_n/V \approx 0.92$ for high bypass ratio engines

5.3.3 Comparison of yawing and OEO sideslip angles

The directional stability of the aircraft for the yawing manoeuvre and the engine failure transient state is described by the equilibrium equation around the vertical axis $\sum M_z = 0$. For the yawing manoeuvres, it is assumed that rudder deflection is the sole contribution, Equation (5.15); conversely for the transient engine out condition, the forces acting over the aircraft are the asymmetric thrust and the wind-milling drag caused by the failed engine with no rudder correction, Equation (5.16).

$$Cn_\beta \beta_{yaw} + Cn_{\delta_R} \delta_R = 0 \tag{5.15}$$

$$Cn_\beta \beta_{OEO} + \underbrace{Cn_{\delta_R} \delta_R}_{0} = -\left(\frac{T_{avail} + D_{mill}}{QS_w}\right)\frac{y_{eng}}{b_w} =$$
$$= -(C_T + C_{D_{mill}})\frac{y_{eng}}{b_w} = -Cn_{OEO} \tag{5.16}$$

where y_{eng} is the lateral coordinate of an engine, T_{avail} is the operative engine thrust available and D_{mill} is the wind-milling drag.

Equations (5.15) - (5.16) result into Equations (5.17) - (5.18). In terms of controllability, this means that the rudder must be able to trim the aircraft for the one-engine-out condition, and therefore the maximum sideslip angle produced by the yawing manoeuvres β_{yaw} will always be greater than the maximum angle encountered at the transient engine-out conditions β_{OEO}.

$$\beta_{yaw} \geq \beta_{OEO} \tag{5.17}$$
$$Cn_{\delta_R} \delta_R \geq Cn_{OEO} \tag{5.18}$$

5.3.4 Maximum rudder deflection

The rudder authority governs the maximum deflection of the yawing control surface, which it is structurally constrained by the lateral force at the VTP and therefore by the dynamic pressure. Then, it is useful to depict the maximum rudder angle versus the airspeed, commonly known as the 'Rudder Travel Limiter' chart.

The handling qualities of the aircraft design the rudder maximum deflection. The aircraft stability must be ensure under two critical conditions for which yawing control is fundamentally used for:

1. Cross-wind landings: to keep the aircraft aligned with the run-way.
2. The engine failure steady state: to sustain a straight flight.

The statistics reveal that 85% of crosswind accidents happen at landing [17]. Cross-wind limitations and operational techniques are applicable by aircraft manufacturers as well as the European Aviation Safety Agency (EASA) to conduct the approach and flare manoeuvres under any runway conditions.

EASA specifies the minimum cross-wind velocity at which safe landing may be conducted. CS/FAR-25.237 states that:

A 90° cross component of wind velocity, demonstrated to be safe for take-off and landing, must be established for dry runways and must be at least 37 km/h (20 kt) or 0.2 V_{SR0}[3], whichever is greater, except that it need not exceed 46 km/h (25 kt).

Despite of this, Airbus describes the maximum demonstrated crosswind at take-off and landing of the aircraft A330-200 to be 33 kts at stabilized conditions with gusts of 40 kts [7].

Considering the cross-wind speed of 33 kts and the estimated minimum approximation airspeed of 110 kts, the aircraft flies at a sideslip angle approximated as:

$$\beta_{xwind} = arcsin\left(\frac{v_{xwind}}{V_{app}}\right) = arcsin\left(\frac{33}{110}\right) \approx 17.5^o \tag{5.19}$$

Applying the equilibrium equation for yawing manoeuvres, Equation (5.15), it is found that a rudder deflection of 31° is required to keep the aircraft stable.

$$\delta_R = -\frac{Cn_\beta}{Cn_{\delta_R}}\beta_{xwind} \tag{5.20}$$

Moreover, the second handling quality condition for which rudder is steadily deflected is the flight with one-engine-out. Aircraft is trimmed to counteract the yawing moment due to the asymmetric thrust of the operative engine and the wind-milling drag of the failed one. In this case, the required rudder angle for null sideslip flight, $\beta = 0^o$, is of the order of 1°, which is less than the corresponding maximum rudder deflection for for a cross-wind condition extrapolated for constant dynamic pressure. The rudder deflection is estimated as:

$$\underbrace{Cn_\beta\beta_{OEO}}_{0} + Cn_{\delta_R}\delta_R = -(C_T + C_{D_{mill}})\frac{y_{eng}}{b_w}$$

$$\delta_R = -\frac{(C_T + C_{D_{mill}})}{Cn_{\delta_R}}\frac{y_{eng}}{b_w} \tag{5.21}$$

---

[3]Reference stall speed in landing configuration

5.3.5   Rudder travel limiter

Having proved that maximum rudder angle occurs at crosswind landings, the rudder travel limiter may be obtained with the assumption of constant dynamic pressure. In other words, it is assumed that the maximum lateral loads at the rudder are obtained at its maximum deflection with Equation (5.20), and the rudder angle curve as a function of the airspeed is computed for constant dynamic pressure with Equation (5.21) in Figure 5.7. Subsequently the sideslip limit angle is obtained from Equation (5.15) in Figure 5.8.
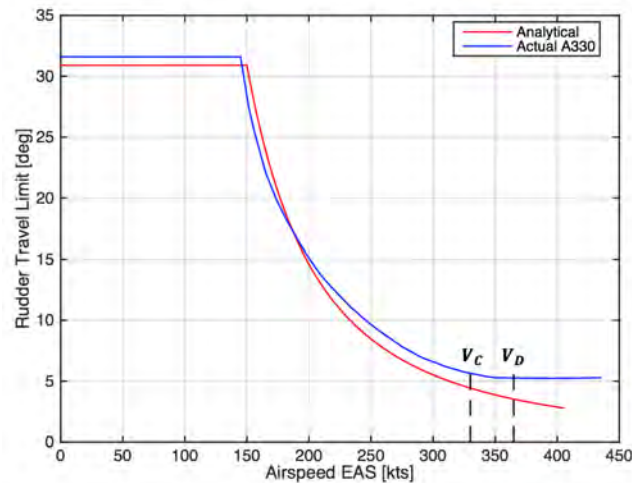
Figure 5.7: *Airbus A330-200 Rudder Travel Limiter*
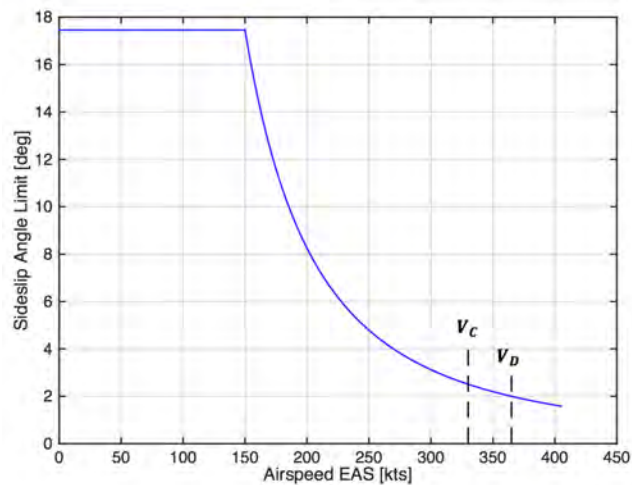
Figure 5.8: *Airbus A330-200 Steady Sideslip Angle Limit*

5.4   Loads' Envelopes

5.4.1   Fuselage reference frame

The loads are provided in the fuselage reference frame. This is, the reference system parallel to the dome reference frame whose origin is located in the fuselage reference line at the dome's locations. The reference system is shown in Figure 5.9, where the height of the dome is $H_{dome} = 7.32$ m. and the radar longitudinal location is $x_{radar} = 33$ m.
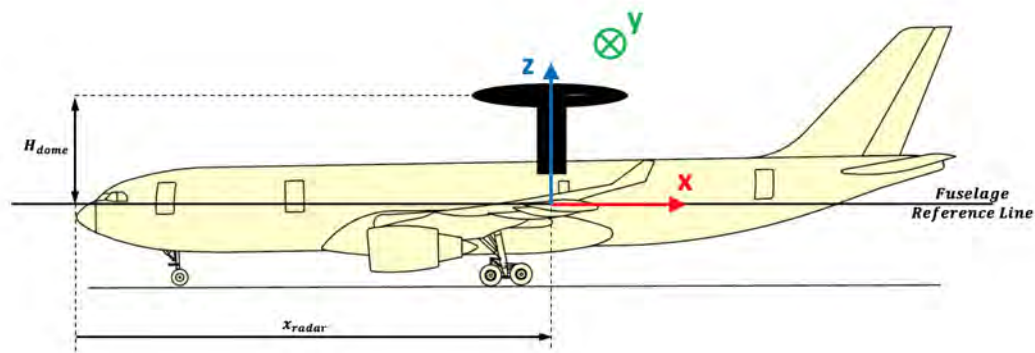
Figure 5.9: *Fuselage reference frame*

From the structural standpoint, this reference system provides more information than the dome reference frame in terms of moments for any future check-stress analysis.

5.4.2   Design loads

The loads are provided as 1D envelopes along with their correlated forces and moments. An envelope refers to the table of maximum/minimum loads' components in each of the reference axis. These envelopes are the result of the sum of aerodynamic and inertial loads for the different flight conditions explained in the previous sections referenced to the fuselage reference frame. Note that the lateral loads, Fy, Mx and Mz, are symmetrized.

These loads are limit loads. Thus, they must be multiplied by a factor of 1.5 to be compared to the emergency landing ultimate loads of Section 5.4.3

Table 5.2: AWACS forces 1D envelope

Fx [N]		Fy [N]	Fz [N]	
Max	**Min**	**Max/min**	**Max**	**Min**
23546	-22908	-48997	57279	-34400

Table 5.3: AWACS correlated loads for max/min forces

	Fx		Fy	Fz	
	Max	**Min**	**Max/min**	**Max**	**Min**
Fx [N]	**23546**	**-22908**	-8826	-22289	5485
Fy [N]	-35703	781	**-48997**	367	-721
Fz [N]	-204	56815	-668	**57279**	**-34400**
Mx [N*m]	120199	-4059	155207	-1608	3918
My [N*m]	154684	811241	-40726	815245	558288
Mz [N*m]	20921	-348	29435	-347	314

Table 5.4: Flight conditions for the forces 1D envelope

	Fx Max	Fx Min	Fy	Fz Max	Fz Min
Speed [KEAS]	404.97	254.02	149.99	254.02	365.00
Altitude [ft]	0.00	0.00	0.00	0.00	41000.00
Q [Pa]	26583.86	10459.29	3646.62	10459.29	14240.25
Ny [-]	-0.24	0.00	±0.36	0.00	0.00
Nz [-]	0.00	2.50	0.00	2.50	2.50
Alpha [deg]	0.00	16.74	0.00	16.74	6.73
Beta [deg]	1.59	0.00	±17.46	0.00	0.00

Table 5.5: AWACS moments 1D envelope

Mx [N*m]	My [N*m]		Mz [N*m]
Max/min	Max	Min	Max/Min
155207	811241	-296892	29435

Table 5.6: AWACS correlated loads corresponding to max/min moments

	Mx	My		Mz
	Max/min	Max	Min	Max/Min
Fx [N]	-8826	-22908	14867	-8826
Fy [N]	-48997	781	-3259	-48997
Fz [N]	-668	56815	-21809	-668
Mx [N*m]	**155207**	-4059	17375	155207
My [N*m]	-40726	**811241**	**-296892**	-40726
Mz [N*m]	29435	-348	1433	**29435**

Table 5.7: Flight conditions for the moments 1D Envelope

	Mx	My Max	My Min	Mz
Speed [KEAS]	149.99	254.02	329.97	149.99
Altitude [ft]	0.00	0.00	0.00	0.00
Q [Pa]	3646.62	10459.29	17649.64	3646.62
Ny [-]	±0.36	0.00	0.00	±0.36
Nz [-]	0.00	2.50	-1.00	0.00
Alpha [deg]	0.00	16.74	-3.97	0.00
Beta [deg]	±17.46	0.00	0.00	±17.46

5.4.3   Emergency Landing Conditions

The emergency landing conditions correspond to the prescribed loads that the aircraft structure must sustained to provide each passenger a reasonable time to escape in a minor crash landing, as described by CS/FAR-25.561(b). The emergency landing loads are ultimate loads.

The following inertial accelerations must be considered to act separately on the structure:

  (i) Upward, $3g$

 (ii) Forward, $9g$

(iii) Sideward, $3g$ on the airframe.

(iv) Downward, $6g$

 (v) Rearward, $1.5g$

Table 5.8: Inertial ultimate forces in Emergency Landing conditions

	Fx [N]		Fy [N]	Fz [N]	
	Max	**Min**	**Max/Min**	**Max**	**Min**
TOTAL	86767	-520604	±173535	173535	-347069
Contributions from:					
DOME	84463	-506780	±168927	168927	-337853
STRUT LH	1152	-6912	±2304	2304	-4608
STRUT RH	1152	-6912	±2304	2304	-4608

The regulations only state the inertial load factors, however non-zero moment contributions exist when forces are applied to their own centre of gravity with respect the fuselage reference frame as noticed in Table 5.9.

Table 5.9: Inertial ultimate moments in Emergency Landing conditions

	Mx [N*m]	My [N*m]		Mz [N*m]
	Max/Min	**Max**	**Min**	**Max/Min**
TOTAL	1105625	560717	-3364304	0
Contributions from:				
DOME	1105625	552813	-3316875	0
STRUT LH	±7905	3952	-23714	∓8557
STRUT RH	∓7905	3952	-23714	±8557

5.4.4   Comparison of loads

According to CS/FAR-25.301(a) the strength requirements are provided in terms of limit loads. These loads involve no structural permanent deformation. On the other hand, ultimate loads are described as the limit loads multiplied by a safety factor of 1.5 and they must be withstand without structural failure. Therefore, the structural stress design criteria for both types of loads is different.

Design loads are specified as limit loads while the Emergency Landing loads are defined as ultimate loads. This means that design loads are multiplied by a safety factor of 1.5 in order to be compared to emergency loads in Figures 5.10 - 5.11 in terms of ultimate loads.

Figure 5.10: *Force comparison of design loads and Emergency Landing loads in terms of ultimate loads*

Figure 5.11: *Moments comparison of design loads and Emergency Landing loads in terms of ultimate loads*

Chapter 6

Fuselage Loads

From the loads' standpoint, the main consequences of having a dome radar over the aircraft are the incremental loads transmitted to the rear fuselage. The loads not only affect the frames' strength of the fuselage but also the empennage surfaces, horizontal and vertical tail-plane, since the aeroplane's static equilibrium must be ensured under all in-flight conditions.

In this chapter, the forces acting on the rear fuselage are computed and the impact of the incremental loads of the radar AWACS over the fuselage are shown.

6.1   Rear Fuselage Loads

The rear fuselage refers to the segment comprised between the wing rear-spar and the tail tip. This section of the aircraft is regarded as a fixed-free cantilever beam, and the loads are computed as so.
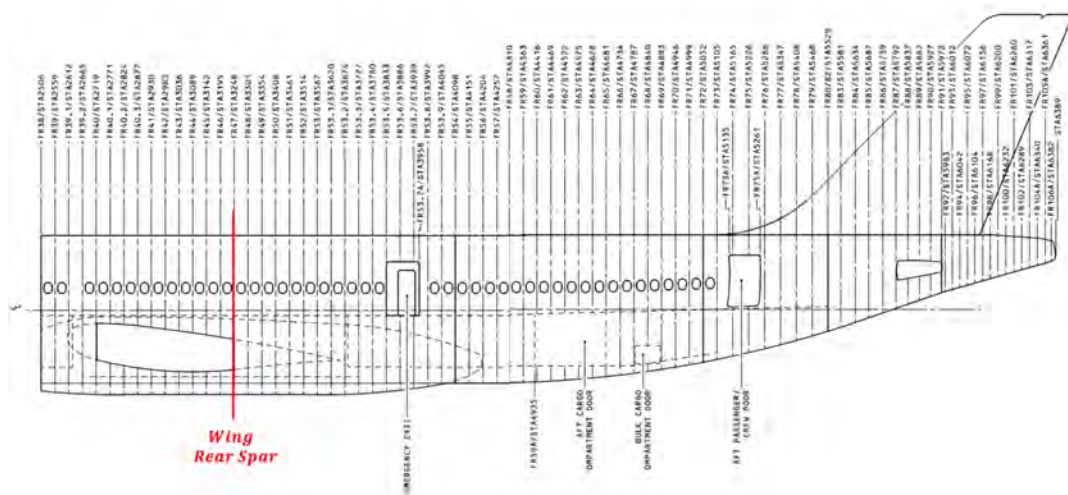
Figure 6.1: *Rear fuselage frames of the Airbus A330-200, Airbus [3]*

The in-fight loads acting on the rear fuselage are divided into:

1. Aerodynamic forces
2. Inertial gravity forces

6.1.1   Aerodynamic Forces

The aerodynamic forces acting on the rear fuselage are the horizontal tail lift, the vertical tail lateral force and the fuselage lateral force. The drag contribution of the empennage surfaces is assumed to be negligible for this analysis.

The horizontal tail lift coefficient is estimated from Torenbeek [45] as a function of the tail efficiency $\eta_h = 0.85$, the HTP mean aerodynamic chord MAC_h and assuming trimmed conditions $C_{m_{ac}} = 0$.

$$C_{L_h} = \frac{C_{m_{ac}} MAC_h Q S_{ref} + N_z W (x_{cg} - x_{ac})}{\eta_h Q S_{ref} (x_{ac} - x_{ac_h})} \tag{6.1}$$

Where MAC_h is estimated as:

$$MAC_h = \frac{2}{3} C_{r_h} (1 + \lambda_h - \frac{\lambda_h}{1 + \lambda_h}) \tag{6.2}$$

being C_{r_h} the horizontal tail root chord and λ_h the taper ratio.
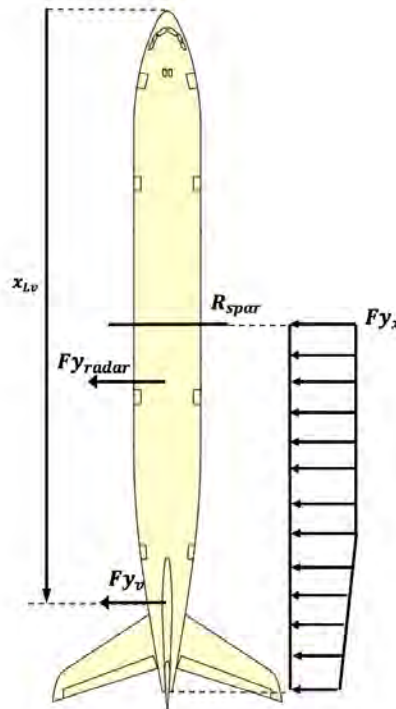
Figure 6.2: *Lateral loads distribution along the rear fuselage, Airbus [2]*

The vertical tail lateral force Fy_v is computed from the VTP lateral force coefficient Cy_{β_v} and the maximum sideslip condition shown in Figure 5.8:

$$Fy_v = -QS_{ref}Cy_{\beta_v}\beta \tag{6.3}$$

Where Cy_{β_v} coefficient is computed from Roskam [38] in Appendix Section C.1.

The fuselage lateral force Fy_{fus} is proportional to the fuselage lateral force coefficient $Cy_{\beta_{fus}}$ and the maximum sideslip condition shown in Figure 5.8:

$$Fy_{fus} = -QS_{ref}Cy_{\beta_{fus}}\beta \tag{6.4}$$

Where $Cy_{\beta_{fus}}$ is computed from Roskam [38] in Appendix Section C.1.

Finally the fuselage lateral force distribution Fy_x is estimated as a function of the wetted lateral surface S_{lat} of the rear fuselage, which varies with the longitudinal location.

$$Fy_x(x)) = \frac{Fy_{fus}}{S_{lat}(x)} \tag{6.5}$$

Where $S_{lat}(x)$ is estimated as:

$$S_{lat}(x) = \begin{cases} d_{fus}(x - x_{R_{spar}}) & \text{for} \quad x \leq x_{\theta_0} \\ \frac{1}{2}(d_{fus} - (x - x_{\theta_0})\tan(\theta_0) + d_{tip})(l_{fus} - x) & \text{for} \quad x > x_{\theta_0} \end{cases} \tag{6.6}$$
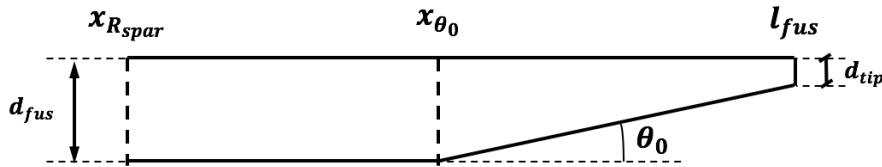
Figure 6.3: *Lateral rear fuselage wetted area simplification*

6.1.2 Inertial gravity forces

The inertial loads involve the forces due to the fuselage structure, the airframe equipment and the empennage weight. The calculation of the mass distributions is explained in detail in Appendix D and the free body diagram is shown in Figure 6.4.

The fuselage mass distribution is computed as the sum of the total fuselage mass divided by the fuselage length and includes:

1. Fuselage structure
2. Systems group: including the flight controls, the pneumatic and hydraulic system, electrical instrumentation and avionics.

3. Furnishing provisions: galleys, seats, oxygen system, evacuation and paint.

The empennage is composed by the horizontal and the vertical tail. The masses of each of them are treated as punctual loads acting on the fuselage at the corresponding frame locations, x_h and x_v respectively.
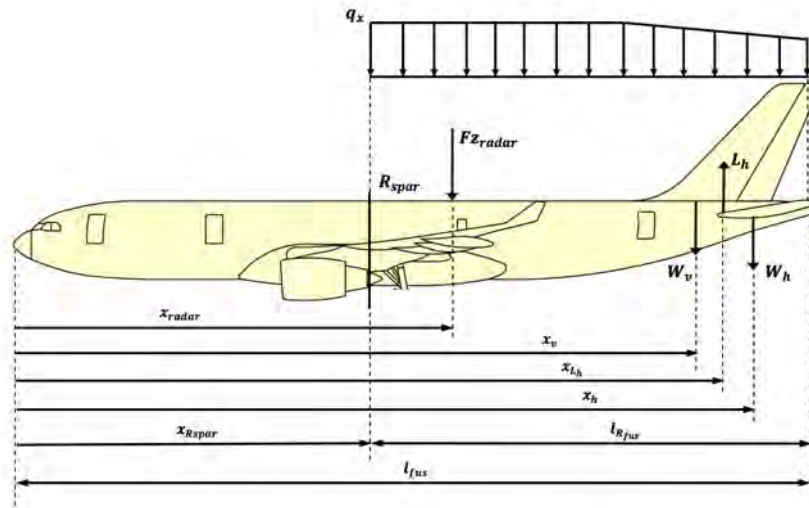
Figure 6.4: *Vertical loads distribution along the rear fuselage, Airbus [2]*

6.1.3   Incremental trimming loads

The incremental trimming loads are the empennage loads needed to ensure the aircraft static balanced due to the presence of the radar. The radar incremental forces and moments must be counteracted by the action of the vertical and horizontal tail so that the static moments around the aircraft centre of gravity are null.

For the vertical tail, the incremental lateral force is:

$$\sum_i Mz = 0 \tag{6.7}$$

$$\Delta Fy_v = -\frac{(\Delta Mz_{cg})_{radar}}{l_v} \tag{6.8}$$

Where l_v is the longitudinal arm between the aircraft CG and the centre of pressure of the vertical tail.

For the horizontal tail, the incremental vertical force is:

$$\sum_i My = 0 \tag{6.9}$$

$$\Delta Fz_h = \frac{(\Delta My_{cg})_{radar}}{l_h} \tag{6.10}$$

Where l_h is the longitudinal arm between the aircraft CG and the centre of pressure of the horizontal tail.

6.2   Fuselage Loads' Distributions

The following figures represent the lateral and vertical force and moment distribution along the rear fuselage of the aircraft. Two load distributions are plotted in each graph, the blue one represents the loads of the operating empty weight of the aircraft A330-200 with zero fuel, no payload nor radar installed; and the red one includes the incremental loads of the radar plus the trimming loads from the empennage.

In the lateral case, F_y and M_z, the design case is the steady flight at maximum sideslip angle as given by Figure 5.8. Note that loads are symmetrized.
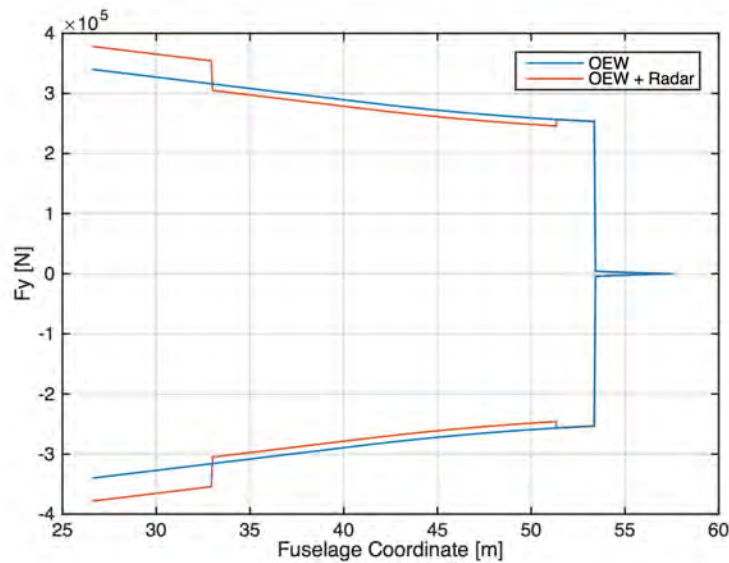
Figure 6.5: *Lateral force along the rear fuselage*
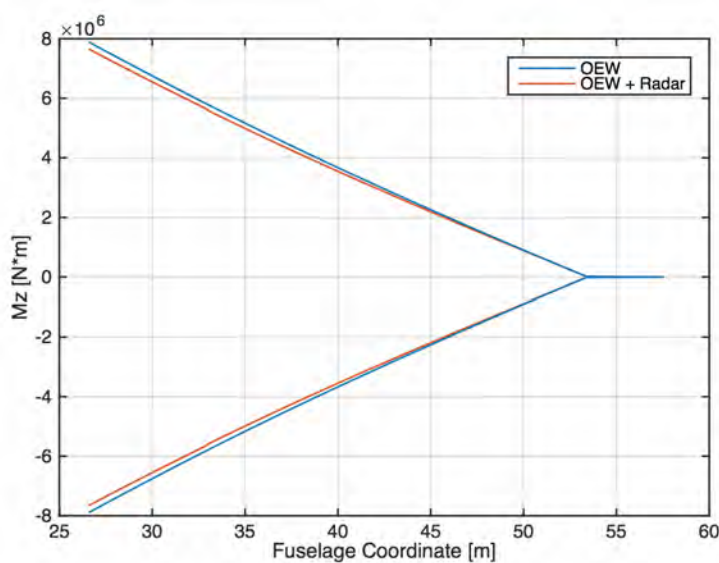
Figure 6.6: *Moment around Z-axis along the rear fuselage*

61

In the longitudinal case, F_z and M_y, the design case in the Balanced Nz conditions. Then, the maximum and minimum vertical load factors are $N_z = 2.5$ and $N_z = -1$ respectively.
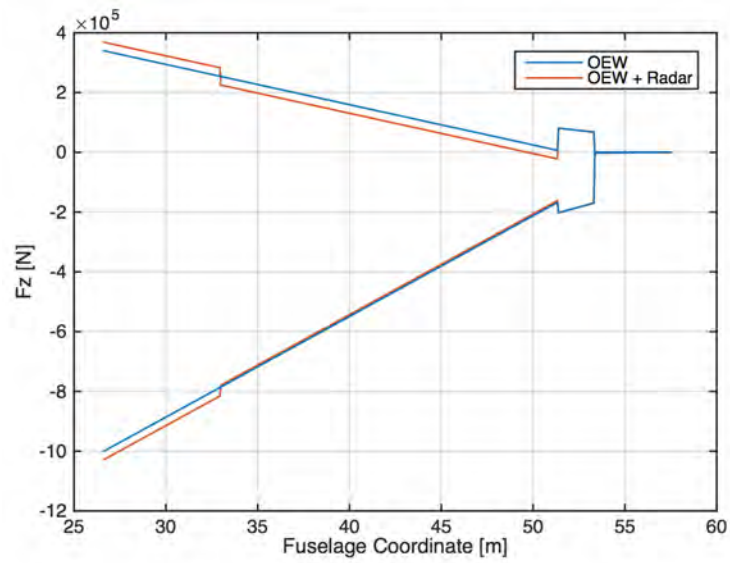
Figure 6.7: *Vertical force along the rear fuselage*
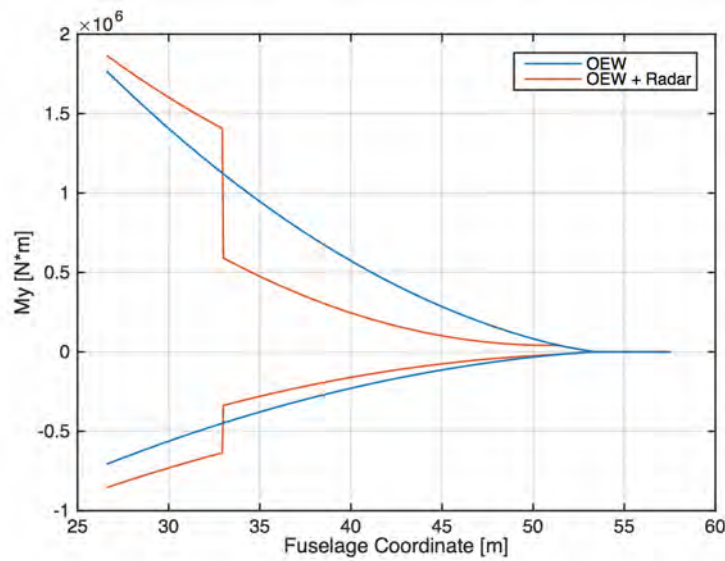
Figure 6.8: *Moment around Y-axis along the rear fuselage*

6.3   Sidewash Effect over the Vertical Tail

The dome and struts of the radar produce a wake at any flight condition. This is specially relevant when flying at a given sideslip angle because it affects the overall performance of the vertical tail, and therefore, the directional stability of the aircraft.

The sidewash angle is the distortion of the sideslip angle that the tail sees compared to the one the aircraft is flying at. It is caused by the aerodynamic interference of the wing which induced an inwards vortex at the tip as illustrated in Figure 6.9. The main consequence over the tail is an increase on the lateral force of the control surface which implies an increase of the restoring yawing moment of the aircraft C_{n_β}.
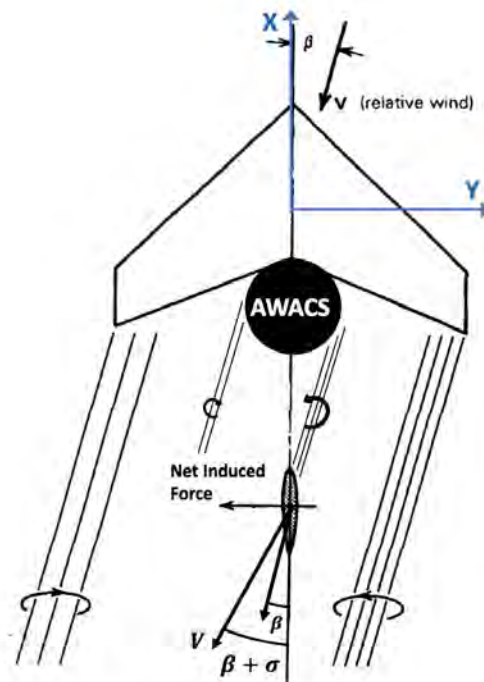
Figure 6.9: *Sidewash angle distortion due to wing interference (top-view), Etkin [16]*

Mathematically, the sidewash angle, σ, is approximated as a linear function of the sideslip angle:

$$\sigma_v = \cancel{\sigma_0}^{0} + \frac{\partial \sigma}{\partial \beta} \cdot \beta \tag{6.11}$$

Then the sideslip angle at the vertical tail β_v can be written as the join contribution of the wing and fuselage body factor and the radar factor,

$$\beta_v = \beta + \sigma_v = \beta + \frac{\partial \sigma}{\partial \beta} \cdot \beta$$

$$= \left(1 + \left[\frac{\partial \sigma}{\partial \beta}\right]_{total}\right) \cdot \beta = \left(1 + \left[\frac{\partial \sigma}{\partial \beta}\right]_{w+f} + \left[\frac{\partial \sigma}{\partial \beta}\right]_{radar}\right) \cdot \beta \tag{6.12}$$

The general equation for the lateral lift force of the vertical tail with no rudder deflection is shown in (6.13), which follows the sign convention shown in Figure 6.9.

$$Y_v = Cy_{\beta_v} Q_v S_v \beta_v = Cy_{\beta_v} Q_v S_v \left(1 + \left[\frac{\partial \sigma}{\partial \beta}\right]_{total}\right) \cdot \beta \qquad (6.13)$$

where Cy_{β_v} is the lift slope of the vertical tail, Q_v is the dynamic pressure at the vertical tail and S_v the surface area of the vertical tail.

Equation 6.13 can be non-dimensionalised as follows,

$$\begin{aligned}
Cy_v &= \frac{Y_v}{QS_{ref}} \cdot \frac{Q_v S_v}{Q_v S_v} \\
&= \frac{S_v}{S_{ref}} \cdot Cy_{\beta_v} \left(1 + \left[\frac{\partial \sigma}{\partial \beta}\right]_{total}\right) \eta_v \cdot \beta \\
&= \frac{S_v}{S_{ref}} \cdot Cy_{\beta_v} \left(1 + \left[\frac{\partial \sigma}{\partial \beta}\right]_{w+f} + \left[\frac{\partial \sigma}{\partial \beta}\right]_{rad}\right) \eta_v \cdot \beta
\end{aligned} \qquad (6.14)$$

where $\eta_v = \frac{Q_v}{Q_\infty}$ is the dynamic pressure ratio.

Concisely, it is useful to look at the lateral force derivative Cy_β,

$$\begin{aligned}
Cy_{\beta_{vtp}} &= \frac{\partial Cy_{vtp}}{\partial \beta} = \\
&= \frac{S_v}{S_{ref}} \cdot Cy_{\beta_v} \left(1 + \left[\frac{\partial \sigma}{\partial \beta}\right]_{w+f} + \left[\frac{\partial \sigma}{\partial \beta}\right]_{rad}\right) \eta_v
\end{aligned} \qquad (6.15)$$

The combined effect of the sidewash due to the wing interference plus the fuselage body and the dynamic pressure ratio is estimated from Equation 5.4.1-a in USAF Datcom [48]:

$$\left(1 + \left[\frac{\partial \sigma}{\partial \beta}\right]_{w+f}\right) \eta_v = 0.724 + 3.06 \cdot \frac{\frac{S_v}{S_{ref}}}{1 + \cos(\Lambda_{w_{c/4}})} + 0.4 \cdot \frac{z_w}{d_{fus}} + 0.009 \cdot AR_w$$

$$(6.16)$$

where Z_w is the vertical distance from the wing root quarter-chord point to the fuselage centre line, positive downwards. The sidewash wing-fuselage interference factor is usually greater than 1 for low-wing aircraft configurations.

Following the same reasoning for the radar, it is assumed the ellipsoidal dome and struts acts as a wing. Thus, the sidewash interference over the vertical tail could lead to a change in the sideslip angle depending on the sidewash derivative factor $[\partial \sigma / \partial \beta]_{radar}$

In sight of the last statement, it is possible to quantify the change in the VTP lateral force Y_{vtp} for a given sideslip angle β by studying the radar sidewash derivative factor with Equation (6.15).

$$\frac{Y_{vtp}}{Y^*_{vtp}} = \frac{Cy_{\beta_{vtp}}}{Cy^*_{\beta_{vtp}}} = \frac{\left(1 + \left[\frac{\partial \sigma}{\partial \beta}\right]_{w+f} + \left[\frac{\partial \sigma}{\partial \beta}\right]_{rad}\right)\eta_v}{\left(1 + \left[\frac{\partial \sigma}{\partial \beta}\right]_{w+f}\right)\eta_v} =$$

$$= 1 + \frac{\left[\frac{\partial \sigma}{\partial \beta}\right]_{rad}\eta_v}{\left(1 + \left[\frac{\partial \sigma}{\partial \beta}\right]_{w+f}\right)\eta_v} \tag{6.17}$$

where Y^* denotes a clean aircraft configuration with no radar installed.

Furthermore, Equation (6.17) allows to estimate the change in the bending moment at the VTP root, and therefore, the increment at the fuselage. Defining the bending moment Mx at the VTP root as the lateral force by the vertical distance of the centre of pressure:

$$Mx_{vtp} = Y_{vtp} \cdot Z_{MAC_v} =$$
$$= Cy_\beta QS_{ref}\beta_{vtp} \cdot Z_{MAC_v} \tag{6.18}$$

The bending moment change is obtained as:

$$\frac{Mx_{vtp}}{Mx^*_{vtp}} = \frac{Cy_{\beta_{vtp}}}{Cy^*_{\beta_{vtp}}} =$$

$$= 1 + \frac{\left[\frac{\partial \sigma}{\partial \beta}\right]_{rad}\eta_v}{\left(1 + \left[\frac{\partial \sigma}{\partial \beta}\right]_{w+f}\right)\eta_v} \tag{6.19}$$

where Mx^* denotes a clean aircraft configuration with no radar installed.

Therefore, for a given sideslip angle all reduces to quantify the radar sidewash derivative factor. A positive factor would indicate that the sideslip angle seen by the tail is greater than the aircraft is flying and both, the lateral loads and the root bending moment, would be higher. On the other hand, a negative factor would denote a reduction of the loads transferred to the fuselage.
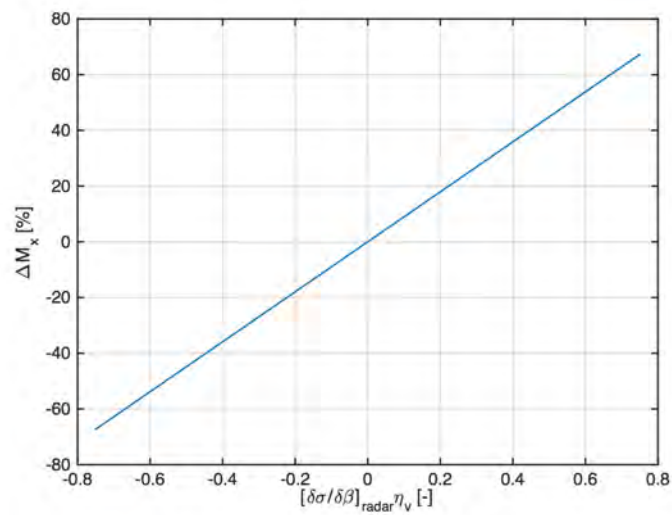
Figure 6.10: *Incremental of Bending Moment Mx at the root of the VTP as a function of the sidewash interference factor of the radar for a given sideslip flight condition*

Chapter 7

Conclusion

7.1 Objectives

Several conclusions can be inferred from the objectives achieved during the project, comprised by one main objective and various secondary objectives.

- **Primary objective**. The main objective of the thesis is to present the methodology to make a preliminary estimation of the static loads generated by a dome AWACS radar mounted on top of the fuselage.

  The aerodynamic and inertial models are used to evaluate the design loads of the radar in Chapter 5. The forces and moments are calculated according to the current civil regulations CS/FAR-25 which describe the flight conditions the aircraft must be able to withstand. In conclusion, the balanced N_z conditions dimension the AWACS symmetrical loads, while the yawing manoeuvres are the most critical for the lateral loads.

  As a final result, a comparison between the emergency landing loads and design loads is presented in terms of ultimate loads. Emergency loads are in most of the cases higher than the design loads. However, this comparison is merely informative because from the structural standpoint, they are two different types of loads (ultimate and limit loads respectively) and therefore the structural design criteria is not the same. In conclusion, both, manoeuvring and emergency landing loads, must be taken into account when performing the structural check-stress analysis bearing in mind that the criteria to analyse the results will be different: permanent elastic deformation for the limit loads and structural failure for the ultimate loads.

- **Secondary objectives**. The secondary objectives are deduced from the main objective and they are summarized below:

  - The incremental loads in the rear fuselage of the aircraft are evaluated in Section 6.1. The evaluation is more qualitative than quantitative and it gives an idea of the expected load distribution after installing the radar. Both, the lateral and vertical loads, tend

to be decreased for the fuselage section between the radar and the empennage, while they increase between the wing rear spar and the radar section.

– An analytical approach is developed in Section 6.3 to estimate the effect of the radar over the vertical tail in terms of loads. The methodology takes into account the side-wash effect generated by the dome which shall be modelled in further advancements.

– A historical survey of AWACS dome radars is conducted in Chapter 2 with the aim to infer some statistical trends from previous dome designs. This study proved to be a useful source to design the radar dimensions for this project.

7.2   Future considerations

A preliminary estimation of the loads resulted from the flight conditions applied and the models developed during the thesis. However, there exists some considerations if further refinements want to be implemented.

First of all, the validity of the aerodynamic model computed in Section 4.2 needs to be proven. CFD numerical simulations are a practical and relatively cheap way of developing an aerodynamic model, nevertheless the author is aware of its limitations. This is why, wind tunnel tests and flight tests must be performed to compare with the numerical results and to correct the aerodynamic coefficients accordingly.

Furthermore, the aerodynamic model was developed for a given Mach number and altitude. Ideally several models for different combinations of Mach number and altitudes inside the flight envelope should be developed because it is known that the aerodynamic coefficients vary according to the Reynolds number and due to compressibility effects.

Regarding the structure, the aeroelastic effects have not been taken into account. The elastic deformation of the structure would affect the pressure distributions over the dome and struts surfaces and therefore the aerodynamic forces and moments. An aeroelastic model considering the structure stiffness should be developed to estimate the incremental loads derived from this effect.

As a final remark, a parametric study of different design variables may help to optimize the aerodynamic performance and to reduce the loads. As stated in Castaño et al. [9], the selected airfoil profile for the struts has an impact on the drag force. The same considerations could be applied for the dome profile and its tilt with respect to the horizontal line. These last parameters not only depend on the aerodynamics, but also in the electronics of the radar and its scanning characteristics which are out of the scope of this research.

Chapter 8

Socioeconomic Context

8.1 Overview

The economical impact of an AWACS radar is not easy to quantify because of the military confidentiality, but in general, it is considered to be very important for both, the contractor companies and the countries involved.

The structural impact of the radar itself would require the modification of several parts of the base aircraft, including the strengthen of the fuselage frames as well as the installation of all the electric and hardware equipment for its working operation. Overall the estimated cost of an AWACS aircraft as the Boeing 707 E3-Sentry was estimated to be $270 millions per unit in FY1998 according to the United States Air Force [47]. That price is 7 times the cost of a civil Boeing 707, estimated in $38.5 millions. The difference gives an order of magnitude of the manufacturing costs of the AWACS system. The United States ordered 33 of those aircraft, therefore the initial investment was around $9,000 millions. The maintenance operational costs must be added to that figure. According to the President's Budget for the FY2016 [13], the E3-Sentry AWACS program enterprise requires an operating and support annual cost of $1.7 millions per aircraft.

An easier value to work with is the costs per flight hour. According to Thompson [43], the operational cost of keeping airborne the Boeing E3-Sentry is $39,587 per flight hour as of 2014. That figure includes the fuel costs estimated at $5,517 per flight hour as shown in Table 8.1 and a salary cost for the aircrew of $3,465, broken-down into 4 flight crew and 17 AWACS specialists [8] as shown in Table 8.2.

Despite of the high developing costs of such a system, the military program can be regarded as a long-term investment. Once the technology has proven its reliability it can be sold to foreign governments. For instance, the E3-Sentry program has been sold to NATO (17 aircraft), to the United Kingdom (7 aircrafts), to Saudi Arabia (5 aircrafts) and France (4 aircrafts). Each of those contracts last for several years and include the maintenance and future upgrades of the aeroplanes. In terms of revenue, major mission updates were installed in 2006 in the NATO fleet as part of the $1,320 millions contract,

Ostrove [36] and United Kingdom support contract is valued $1,300 million over 21 years.

Table 8.1: Boeing E3-Sentry fuel cost per flight hour [$/h]

Fuel capacity[1] [US gal]	21000	
Fuel Jet A[2] [$/gal]	2.89	
Total fuel cost [$]		60,690
Endurance [h]	11	
Fuel cost per flight hour [$/h]		5,517

Table 8.2: Aircrew salary cost per flight hour

Crew	21	
Salary per hour[3] [$/h]	15	
Flight Hours [h]	11	
Salary cost per flight hour [$/h]		3465

8.2 Project's budget

The budget for the present Bachelor's Thesis takes into account the direct and indirect costs related to the accomplishments of the project. The direct costs refer to those related to the accomplishment of the project and include the labour cost associated to the Aerospace engineer work, estimated to be 20 per hour, and the equipment costs. These costs comprise the software licenses required for the CFD simulation and the data processing as well as the computer. The indirect cost considered is the electricity, which assumes a computer power consumption of 90 Watts per hour.

The budget is contained in Table 8.3.

---

[1]US Air Force [47]
[2]As of 2014, Energy Information Administration [14]
[3]Salary for E5 Army Sergeant [40]

Table 8.3: Project's budget

CONCEPT	HOURS	COST		TOTAL	
Software					
MATLAB Academic License		500	€		
ANSYS CFX Research License		2500	€		
Hardware					
Computer		1500	€		
TOTAL EQUIPMENT				4500	€
Labour [hour]					
Bibliographic Research	15	h			
ANSYS Learning	20	h			
CAD Modelling	50	h			
Data Processing	100	h			
Documentation	90	h			
Meetings	15	h			
Working hours	290	h			
TOTAL LABOUR COST (20€/h)				5800	€
CFD Simulation	500	h			
Total hours	790	h			
Electricity (0.12€/kwh)				8.37	€
TOTAL COST				**10,308.37**	€

Bibliography

[1] *8 Squadron History - The Nimrod AEW Saga*. 2006. URL: http://www.8squadron.co.uk/history%7B%5C_%7Dnimrod.php (Retrieved: 06/18/2017).

[2] Airbus. *A330 Aircraft characteristics: Airport and maintenance planning*. Tech. rep. Blagnac, France, 2017.

[3] Airbus. *A330 Aircraft Recovery Manual*. Tech. rep. Blagnac, France, 2009.

[4] ANSYS Inc. "ANSYS CFX-Solver Theory Guide 16.2.3". In: (2015).

[5] Sergio Arocha. *El 'súper radar' capaz de controlar una batalla aérea — Tecnology Militar*. 2015. URL: https://tecnologamilitar.blogspot.com.es/2015/02/el-super-radar-capaz-de-controlar-una.html (Retrieved: 06/18/2017).

[6] Michael Baldock. *Westland WS-61 Sea King ASaC7 - UK - Navy — Aviation Photo #0681322 — Airliners.net*. 2004. URL: http://www.airliners.net/photo/UK-Navy/Westland-WS-61-Sea-King-ASaC7/681322 (Retrieved: 06/18/2017).

[7] BFU. *Investigation Report - A320 Crosswind Landing*. Tech. rep. March. Hamburg: German Federal Bureau of Aircraft Accident Investigation, 2010, p. 85.

[8] Boeing. *E-3 Airborne Warning and Control System (AWACS)*. Tech. rep. Boeing Defense Space & Security, 2012, p. 5. URL: www.boeing.com/assets/pdf/defense-space/ic/awacs/docs/E-3AWACS%7B%5C_%7Doverview.pdf.

[9] Noel Castaño Sanchez, Ernesto Rodriguez Cisneros, and Emilio Angel Blasco. "C-295 AEW Aerodynamic Design Process: CFD, wind tunnel tests and flight tests". San Diego, CA, 2013.

[10] S. Christopher. "State-of-the-art in active electronically-steered array surveillance radar: Indian value addition". In: *Defence Science Journal* 60.2 (2010), pp. 184–188. ISSN: 0011748X.

[11] Hector Climent Mañez. *Aeroelasticity*. Tech. rep. Universidad Carlos III de Madrid, 2016.

[12] Defensa.com. "India comprará seis aviones para convertirlos en AWACS". In: (2014). URL: http://www.defensa.com/africa-asia-pacifico/india-comprara-seis-aviones-para-convertirlos-awacs.

[13] Department of Defense. *Selected Acquisition Report (SAR) Airborne Warning and Control System Block 40 / 45 Upgrade*. Tech. rep. Department of Defense of the United States, 2015. URL: `www.dod.mil/pubs/foi/.../15-F-0540%7B%5C_%7DAWACS%7B%5C_%7DBlk%7B%5C_%7D40%7B%5C_%7D45%7B%5C_%7DSAR%7B%5C_%7DDec%7B%5C_%7D2014.PDF`.

[14] EIA. *U.S. Gulf Coast Kerosene-Type Jet Fuel Spot Price FOB (Dollars per Gallon)*. 2017. URL: `https://www.eia.gov/dnav/pet/hist/LeafHandler.ashx?n=PET%7B%5C&%7Ds=EER%7B%5C_%7DEPJK%7B%5C_%7DPF4%7B%5C_%7DRGC%7B%5C_%7DDPG%7B%5C&%7Df=M` (Retrieved: 06/20/2017).

[15] Embraer. *DefesaNet - Aviação - E99 - SAAB modernizará Radar Erieye*. 2013. URL: `http://www.defesanet.com.br/aviacao/noticia/9877/e99---saab-modernizara-radar-erieye.jpg` (Retrieved: 06/18/2017).

[16] B Etkin. *Dynamics of flight: stability and control*. John Wiley & Sons Australia, Limited, 1982. ISBN: 9780471089360.

[17] Flight Safety Foundation. "FSF ALAR Briefing Note 7.1- Stabilized Approach". In: *Flight Safety Digest* 17 - 18 (2000), pp. 133–138.

[18] Fuerza Aerea de Chile. *FACH*. URL: `http://www.fach.cl/GALERIA/aviones%7B%5C_%7Dtransporte/boeing%7B%5C_%7D707%7B%5C_%7Dcondor/boeing%7B%5C_%7D707.html` (Retrieved: 06/18/2017).

[19] Aleksey Gerasimov. "Modeling Turbulent Flows with FLUENT". In: ANSYS,lnc., 2006.

[20] Joel Grasmeyer. "Stability and Control Derivative Estimation and Engine- Out Analysis". In: (1998), p. 28.

[21] Hephaestus Aetnaean. *radar - Why is the AWACS' rotodome located at the back and over the aircraft? - Aviation Stack Exchange*. 2015. URL: `https://aviation.stackexchange.com/questions/21860/why-is-the-awacs-rotodome-located-at-the-back-and-over-the-aircraft` (Retrieved: 06/18/2017).

[22] HispanTV. *OTAN protege el cielo de Turquía con aviones AWACS - HispanTV, Nexo Latino*. 2016. URL: `http://www.hispantv.com/noticias/turquia/218470/otan-envia-aviones-awacs-turquia` (Retrieved: 06/18/2017).

[23] Denis Howe. "Aircraft conceptual design synthesis". In: *Professional Engineering* (2000).

[24] *Images — DAHG*. URL: `https://deffordairfieldheritagegroup.wordpress.com/images/` (Retrieved: 06/18/2017).

[25] Frank P Incropera et al. *heat and mass transfer - Incropera 6e*. 2007. arXiv: `1105-`.

[26] Jakartagreater. *Program Belanja Persenjataan Alutsista Republik Indonesia 2012-2019 Berita Terkini Militer Hankam*. 2014. URL: `http://www.militerhankam.com/2014/03/program-belanja-persenjataan-alutsista.html?m=0` (Retrieved: 06/18/2017).

[27] W. P. Jones and B. E. Launder. "The Prediction of Laminarization With aTwo-Equation Model of Turbulence". In: *International Journal of Heat and Mass Transfer* 15.2 (1972), pp. 301–314. ISSN: 00179310.

[28] T. von Kármán. "Mechanical Similitude and Turbulence". In: *NACA TM 611* (1931), p. 22.

[29] Ajoy Kumar Kundu. *Aircraft Design*. 2010, p. 606. ISBN: 9780521885164.

[30] LEAP CFD Team. *Computational Fluid Dynamics (CFD) Blog - LEAP Australia & New Zealand — Tips & Tricks: Inflation Layer Meshing in ANSYS*. 2012. URL: `https://www.computationalfluiddynamics.com.au/tips-tricks-inflation-layer-meshing-in-ansys/` (Retrieved: 06/18/2017).

[31] Ted L Lomax. *Structural Loads Analysis for Commercial Transport Aircraft*. 1996. ISBN: 1563471140 9781563471148.

[32] Florian R Menter. "Influence of freestream values on k-ω turbulence model predictions". In: *AIAA Journal* 30.6 (1992), pp. 1657–1659. ISSN: 0001-1452.

[33] Florian R Menter. "Two-equation eddy-viscosity turbulence models for engineering applications". In: *AIAA journal* 32.8 (1994), pp. 1598–1605. ISSN: 0001-1452.

[34] Florian R Menter. "Zonal Two Equation k-w, Turbulence Models for Aerodynamic Flows". In: *AIAA paper*. 1993, p. 2906. ISBN: 103975.

[35] Northtrop Grumman. *Awacs Surveillance Radar: The Eyes of the Eagle*. Tech. rep. Baltimore, Maryland: Northrop Grumman Corporation, 2015, p. 12. URL: `www.northropgrumman.com/capabilities/awacsapy2/documents/awacs.pdf%7B%5C%%7D5Cn`.

[36] Bill Ostrove. *APY-1 / 2 (V) (AWACS) - Archived 01/2008*. Tech. rep. January 2007. Forecast International, 2007, pp. 1–11. URL: `https://www.forecastinternational.com/archive/disp%7B%5C_%7Dpdf.cfm?DACH%7B%5C_%7DRECNO=337`.

[37] Maria Pester. "Multii-Disciplinary Conceptual Aircraft Design using CEASIOM". PhD thesis. Hamburg: Hamburg University of Applied Science, 2010. ISBN: 0953399192.

[38] J Roskam. *Methods for Estimating Stability and Control Derivatives of Conventional Subsonic Airplanes*. Lawrence, Kansas, 1971.

[39] Russavia. *Kasama Ka*. 2011. URL: `http://photo.wn.com/Kasama%7B%5C_%7DKa` (Retrieved: 06/18/2017).

[40] Salary.com. *E6 - Staff Sergeant (Army) Salaries by education, experience, location and more - Salary.com*. 2017. URL: `http://www1.salary.com/E6-Staff-Sergeant-Army-salaries.html` (Retrieved: 06/21/2017).

[41] Robert Sherman. *E-2C Hawkeye - Military Aircraft*. URL: `https://fas.org/man/dod-101/sys/ac/e-2.htm` (Retrieved: 06/18/2017).

[42] Alan O Sykes. "An Introduction to Regression Analysis". Chicago, 1993.

[43] Mark Thompson. *Costly Flight Hours — TIME.com*. 2013. URL: `http://nation.time.com/2013/04/02/costly-flight-hours/` (Retrieved: 06/20/2017).

[44] E Torenbeek. *Synthesis of Subsonic Airplane Design: An introduction to the preliminary design of subsonic general aviation and transport aircraft, with emphasis on layout, aerodynamic design, propulsion and performance*. Springer Netherlands, 1982, p. 598. ISBN: 9789024727247.

[45] Egbert Torenbeek. *Advanced Aircraft Design: Conceptual Design, Analysis and Optimization of Subsonic Civil Airplanes*. 2013, pp. 1–410. ISBN: 9781118568118.

[46] *Tupolev Tu-126. Foto. Video. Historia. Características.* URL: `http://es.avia.pro/blog/tu-126` (Retrieved: 06/18/2017).

[47] US Air Force. *E-3 Sentry (AWACS) ¿ U.S. Air Force ¿ Fact Sheet Display*. 2015. URL: `http://www.af.mil/About-Us/Fact-Sheets/Display/Article/104504/e-3-sentry-awacs/` (Retrieved: 06/20/2017).

[48] USAF. *Digital Datcom*. 2013. URL: `http://www.pdas.com/datcom.html`.

[49] USAF Test Pilot School. *Chapter 11 Engine-Out Theory*. Tech. rep. California: Edward Air Force Base, 1992, p. 54.

[50] Mali Vijay. *Velocity profiles in turbulent wall flow*. 2016. URL: `https://www.learncax.com/knowledge-base/blog/by-category/cfd/basics-of-y-plus-boundary-layer-and-wall-function-in-turbulent-flows` (Retrieved: 07/28/2016).

[51] Michael J. Wagner. "AEW Aircraft Design". PhD thesis. Naval Postgraduate School, 1992.

[52] A U Weerasuriya. "Computational Fluid Dynamic (CFD) Simulation of Flow around Tall Buildings". In: *Engineer: Journal of the Institution of Engineers, Sri Lanka* 46.3 (2013), pp. 43–54.

[53] *Wellington MkIII RCAF 419Sqn VR Q Z1572 RAF Lakenheath Mildenhall Suffolk 1942 — Vickers — Pinterest — Feste rave e Ricerca*. URL: `https://it.pinterest.com/pin/340655159298984645/` (Retrieved: 06/18/2017).

[54] D.C. Wilcox. "Turbulence modeling for CFD". In: *AIAA Journal* 93 (1993), p. 2905. ISSN: 0022-1120. arXiv: `arXiv:1011.1669v3`.

[55] Jason Xu. *Ilyushin KJ2000 (Il-76MD) - China - Air Force — Aviation Photo #2744091 — Airliners.net*. 2015. URL: `http://www.airliners.net/photo/China-Air-Force/Ilyushin-KJ2000-Il-76MD/2744091` (Retrieved: 06/18/2017).
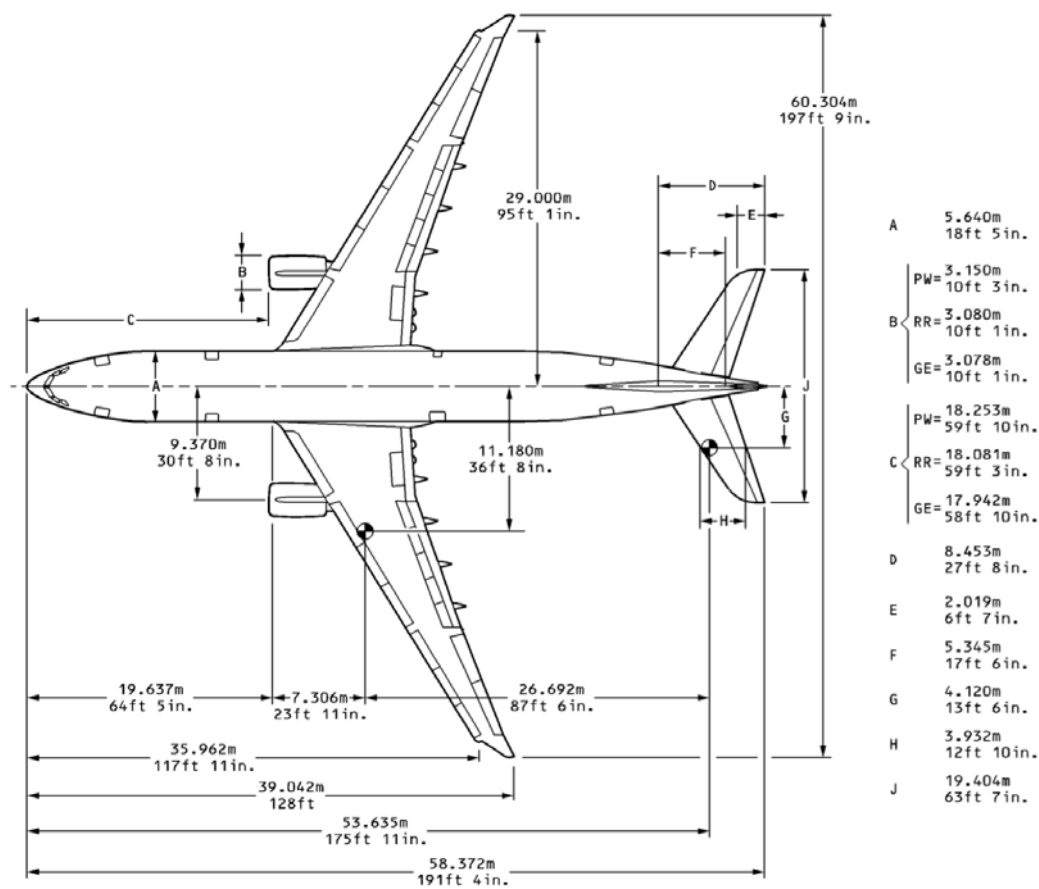
Appendix A

Reference Aircraft

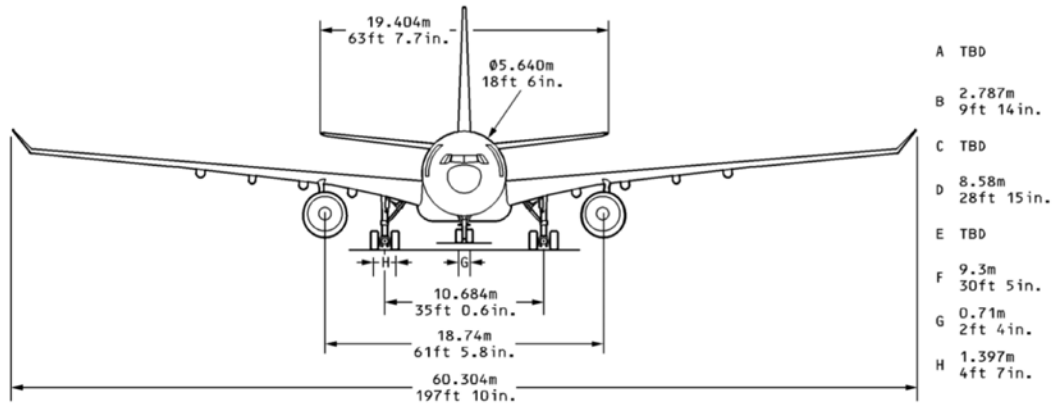Figure A.1: *Aircraft A330-200 top-view dimensions, Airbus [3]*

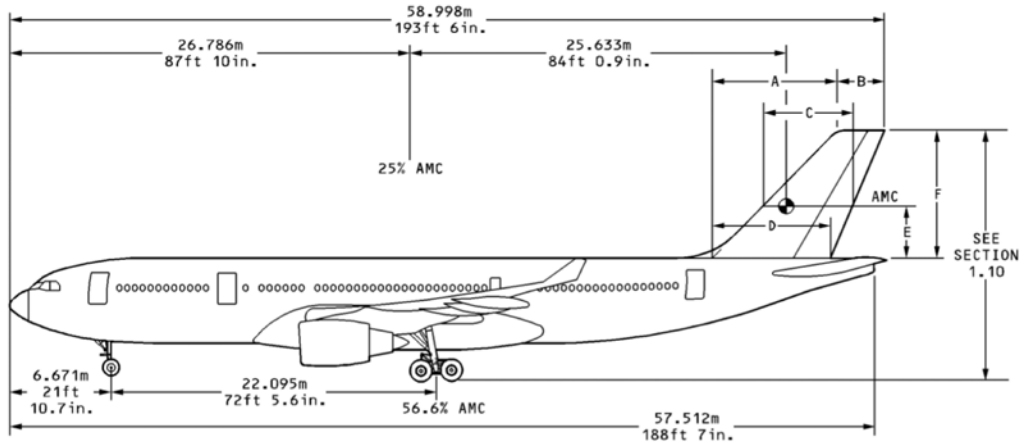Figure A.2: *Aircraft A330-200 front-view dimensions, Airbus [3]*

Figure A.3: *Aircraft A330-200 side-view dimensions, Airbus [3]*

Table A.1: Airbus A330-200 dimensions (I)

AIRCRAFT			
CG Longitudinal Location (25% Wing MAC)	x_{cg}	26.79	m
Maximum Take-Off Weight	$MTOW$	230000	kg
Maximum Zero Fuel Weight	$MZFW$	168000	kg
Maximum Landing Weight	MLW	180000	kg
Operating Empty Weight	OEW	127000	kg
Engine Lateral Coordinate	y_{eng}	9.37	m
Maximum Thrust per engine	T_0	312000	N
WING			
Reference Area	S_{ref}	361.63	m^2
Span	b_w	60.3	m
Mean Aerodynamic Chord	MAC_w	7.27	m
Aspect Ratio	AR_w	9.39	
Tip Chord	c_{t_w}	2.46	m
Root Chord	c_{r_w}	10.56	m
Taper Ratio	λ_w	0.23	
Sweep Angle 25% MAC	Λ_w	30	deg
Rear Spar Location (from nose)	$X_{R_{spar}}$	26.63	m
Vertical distance wing root quarter-chord to fus. line	Z_w	1	m
HORIZONTAL TAIL			
Reference Area	S_h	71.45	m^2
Span	b_h	19.4	m
Mean Aerodynamic Chord	MAC_h	3.93	m
Aspect Ratio	AR_h	5.27	
Tip Chord	c_{t_h}	2.01	m
Root Chord	c_{r_h}	5.35	m
Taper Ratio	λ_h	0.38	
Sweep Angle 25% MAC	Λ_h	30	deg
Distance 25% MAC wing to 25% MAC HTP	l_h	26.85	m

Table A.2: Airbus A330-200 dimensions (II)

VERTICAL TAIL			
Reference Area	S_v	51.39	m^2
Span	b_v	8.8	m
Mean Aerodynamic Chord	MAC_v	6.27	m
Aspect Ratio	AR_v	1.51	
Tip Chord	c_{t_v}	3.1	m
Root Chord	c_{r_v}	8.58	m
Taper Ratio	λ_v	0.36	
Sweep Angle 25% MAC	Λ_v	39.5	deg
Distance 25% MAC wing to 25% MAC VTP	l_v	25.52	m
Vertical distance root to MAC	Z_{MAC_v}	3.71	m
FUSELAGE			
Length	l_{fus}	57.51	m
Rear fuselage length	$l_{R_{fus}}$	26.63	m
Maximum Diameter or Fuselage Width	d_{fus} or W_{fus}	5.64	m
Diameter Tail-Tip	d_{tip}	1	m
Rotation Angle	θ_0	15	deg
Length tubular fuselage	x_{θ_0}	40.96	m
Radar longitudinal location	x_{radar}	33	m
Height of the dome (from fus. reference line)	H_{dome}	7.32	m

Appendix B

Radar Dimensions

The geometric dimensions of the model are taken from the Boeing E3-Sentry radar. These dimensions fit the AWACS design trends presented in Chapter 2.
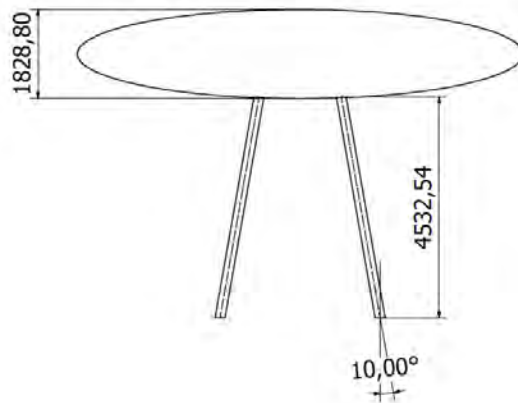

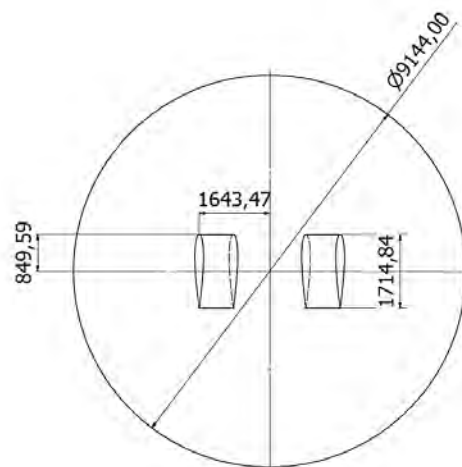Figure B.1: *AWACS radar front-view dimensions in millimetres*

Figure B.2: *AWACS radar bottom-view dimensions in millimetres*

Appendix C

Directional stability and control derivatives

The stability stability and control derivatives for the aircraft Airbus A330-200 are estimated according to the method contained in Roskam [38] and bundled in Grasmeyer, J. [20].

C.1   Sideforce coefficient

The sideforce coefficient variation with the sideslip angle is contributed by the wing, the fuselage and the vertical tail. .

$$Cy_\beta = Cy_{\beta_{wing}} + Cy_{\beta_{fus}} + Cy_{\beta_v} \tag{C.1}$$

The wing contribution is estimated as function of dihedral angle Γ:

$$Cy_{\beta_w} = -0.0001 \left| \Gamma \right| \frac{180}{\pi} \tag{C.2}$$

The fuselage contribution along with the engine nacelles is computed as:

$$Cy_{\beta_{fus}} = -2K_{wbi} \frac{S_o}{S_{ref}} \tag{C.3}$$

The K_{wbi} is the wing-body interference factor obtained from a curve fit to Figure 7.1 in Roskam [38]:

$$
\begin{aligned}
K_{wbi} &= 0.85 \frac{-Z_w}{d_{fus}/2} + 1 & for \quad \frac{Z_w}{d_{fus}/2} < 0 \\
K_{wbi} &= 0.5 \frac{Z_w}{d_{fus}/2} + 1 & for \quad \frac{Z_w}{d_{fus}/2} > 0
\end{aligned}
\tag{C.4}
$$

and the lateral wetted surface of fuselage and nacelles S_o approximated by:

$$S_o \cong \pi \left(\frac{d_{fus}}{2} \right)^2 + N_{engines} \pi \left(\frac{d_{nacelle}}{2} \right)^2 \tag{C.5}$$

F

The vertical tail contribution lateral force is obtained from:

$$Cy_{\beta_v} = -k_{Cy_{\beta,v}} C_{l_{\alpha_{v_{eff}}}} \left(1 + \frac{\partial \sigma}{\partial \beta}\right) \eta_v \frac{S_v}{S_{ref}} \qquad (C.6)$$

where:

$k_{Cy_{\beta,v}}$ is found from a curve fit to Figure 7.3 in Roskam [38]:

$$k_{Cy_{\beta,v}} = 0.75 \qquad\qquad for \quad \frac{b_v}{d_{fus_v}} < 2$$

$$k_{Cy_{\beta,v}} = \frac{1}{6}\frac{b_v}{d_{fus_v}} + \frac{5}{12} \qquad\qquad for \quad \frac{b_v}{d_{fus_v}} < 2 \qquad (C.7)$$

$$k_{Cy_{\beta,v}} = 1 \qquad\qquad for \quad \frac{b_v}{d_{fus_v}} > 3.5$$

The effective lift coefficient of the vertical tail is:

$$C_{l_{\alpha_{v_{eff}}}} = \frac{2\pi A}{2 + \sqrt{\frac{A^2 \beta_M^2}{\kappa^2}\left(1 + \frac{\tan^2 \Lambda_{c/2}}{\beta_M^2}\right)}} \qquad (C.8)$$

$$\kappa = \frac{C_{l_{\alpha_{vtp}}}}{2\pi} \qquad (C.9)$$

β_M is the Prandtl-Glauert Factor:

$$\beta_M^2 = \sqrt{1 - M^2} \qquad (C.10)$$

$$\left(1 + \left[\frac{\partial \sigma}{\partial \beta}\right]\right)\eta_v = 0.724 + 3.06 \cdot \frac{\frac{S_v}{S_{ref}}}{1 + \cos(\Lambda_{c/4})} + 0.4 \cdot \frac{z_w}{d_{fus}} + 0.009 \cdot AR_w \quad (C.11)$$

$$A_{vtp,eff} = \frac{A_V(B)}{A_V} A_{vtp}\left[1 + K_H\left(\frac{A_V(HB)}{A_V(B)} - 1\right)\right] \qquad (C.12)$$

Where:

$\frac{A_V(B)}{A_V}$ is the ratio of aspect ratio of the vertical tail in the presence of the body over the isolated panel. It is determined from Equation (3-16) in Grasmeyer, J. [20] with the curve fit of Figure 7.5 in Roskam [38].

$\frac{A_V(HB)}{A_V(B)}$ is the ratio of aspect ratio of the vertical tail in the presence of the horizontal tail and the body over the one of the body alone. It is assumed to be 1.1 from Figure 7.6 in Roskam [38].

K_H is a factor for the relative size of the horizontal and vertical tails. It is determined from Equation (3-17) in Grasmeyer, J. [20] with the curve fit of Figure 7.7 in Roskam [38].

C.2   Yawing moment coefficient

The yawing moment coefficient variation with the sideslip angle is given by the contributions of the wing, fuselage and vertical tail.

$$Cn_\beta = Cn_{\beta_w} + Cn_{\beta_{fus}} + Cn_{\beta_v} \tag{C.13}$$

The wing contribution to the yawing moment coefficient is neglected for small angles.

$$Cn_{\beta_w} \cong 0 \tag{C.14}$$

The fuselage contribution is found from:

$$Cn_{\beta_{fus}} = -K_N K_{R_l} \frac{S_{bs}}{S_{ref}} \frac{l_{fus}}{b_w} \frac{180}{\pi} \tag{C.15}$$

Where:

K_N is assumed to be 0.0011. It is determined by Figure 7.19 in Roskam.

K_{R_l} is the fuselage Reynolds number estimated with a curve fit from Figure 7.20 in Roskam.

S_{bs} is the fuselage side area. For a Boeing 777 geometry the following approximation is valid:

$$S_{bs} = 0.83 \cdot l_{fus} d_{fus} \tag{C.16}$$

The vertical tail contribution to the yawing moment coefficient is obtained as follows:

$$Cn_{\beta_v} = -Cy_{\beta_v} \frac{l_v \cos(\alpha) + z_v \sin(\alpha)}{b_w} \tag{C.17}$$

Where Cy_{β_v} is computed in Equation C.6

C.3   Sideforce coefficient due to rudder deflection

The derivative of the lateral force coefficient due to a rudder deflection is found from:

$$Cy_{\delta_R} = C_{l_{\alpha_{v_{eff}}}} \frac{(\alpha_\delta)_{C_L}}{(\alpha_\delta)_{C_l}} K' K_b \frac{S_{vtp}}{S_{ref}} \tag{C.18}$$

Where:

$\frac{(\alpha_\delta)_{C_L}}{(\alpha_\delta)_{C_l}}$ is a ratio accounting for the 3D flap effectiveness to the 2D flap effectiveness. It is estimated from Figure 10.2 in Roskam assuming a $c_f/c = 0.33$.

K_b is the flap span factor. It is determined from Figure 10.3 in Roskam with $\Delta\eta = 0.85$.

K' is an empirical correction factor for large control deflections. It is estimate in Figure 10.7 in Roskam.

C.4 Yawing moment coefficient due to rudder deflection

The yawing moment coefficient contribution of rudder is given by:

$$Cn_{\delta_R} = -Cy_{\delta_R} \frac{l_v \cos(\alpha) + z_v \sin(\alpha)}{b_w} \tag{C.19}$$

C.5 Correction factors

Based on the research of Grasmeyer, J. [20] Section 4, the following correction factors are applied to the stability and control derivatives for aircraft geometries of the type Boeing 747-100.

Table C.1: Correction factors for stability and control derivatives

	Correction Factor
Cy_β	1.4068
Cn_β	2.6690
Cy_{δ_R}	0.6132
Cn_{δ_R}	0.7286

Appendix D

Aircraft fuselage and empennage mass distribution

At the conceptual design phases of an aircraft, it is required to work with semi-empirical formulae for the mass estimation of the different components. In particular, this section focuses on the fuselage, airframe equipments and empennage.

D.1 Fuselage structure

The fuselage structural mass is estimated from Torenbeek [44]:

$$M_{fus} = 0.23 \left(V_D \frac{l_{fus}}{b_{fus} + h_{fus}} \right)^{0.5} S_G^{1.2} (1 + k_p + k_c + k_u) \tag{D.1}$$

Where k_p is 0.08, k_c is 0.1 and k_u is 0.07. S_G is the gross shell area of the fuselage estimated as:

$$S_G = \pi b_{fus} l_{fus} \left(1 - \frac{2}{l_{fus}/b_{fus}} \right)^{2/3} \left(1 + \frac{1}{(l_{fus}/b_{fus})^2} \right) \tag{D.2}$$

D.2 Airframe equipment and services

The airframe equipment and services are composed by the systems group and miscellaneous provisions.

$$M_{equip} = M_{sys} + M_{fur} + M_{prov} \tag{D.3}$$

D.2.1 Systems group

Kundu [29] proposal for the systems group includes the flight controls, the pneumatic and hydraulic system, electrical instrumentation and avionics.

$$M_{sys} = k_{sys} \cdot MTOW \tag{D.4}$$

where k_{sys} is 0.11 for large aircraft (pax capacity ¿ 100).

D.2.2 Furnishing and provisions

The furnishing group includes galleys, seats, oxygen system, evacuation and paint. Kundu [29] estimation is:

$$M_{fur} = k_{fur} \cdot MTOW \tag{D.5}$$

where k_{fur} is 0.08 for large aircraft (pax capacity ¿ 100).

Additionally, it is convenient to have a 1% of the MTOW dedicated to provisions for miscellaneous equipment:

$$M_{prov} = 0.01 \cdot MTOW \tag{D.6}$$

D.3 Fuselage mass distribution

The fuselage mass distribution q_x is calculated by dividing the total mass of the fuselage structure and airframe equipments by the corresponding fuselage length.

$$q_x = \frac{M_{fus} + M_{equip}}{l_{fus}} \tag{D.7}$$

D.4 Empennage

The mass of the empennage is divided into the horizontal and the vertical tail. According to Torenbeek [44], they are estimated as:

$$M_{tail} = M_v + M_h \tag{D.8}$$

The mass of the vertical tail is computed as:

$$M_h = S_h k_h f_y (x_h) \tag{D.9}$$

where k_h is 1.1 for variable incidence tails, otherwise 0. x_h is obtained by:

$$x_h = \frac{S_h^{0.2} V_D / 1000}{\sqrt{cos(\Lambda_{h,0.5})}} \tag{D.10}$$

The mass of the horizontal tail is estimated as:

$$M_v = S_v k_v f_y (x_v) \tag{D.11}$$

where k_v is 1 for fuselage-mounted horizontal tail; otherwise, for fuselage-mounted at height h_h is $k_v = 1 + 0.15\frac{S_h h_h}{S_v h_v}$. x_v is obtained by:

$$x_v = \frac{S_v^{0.2} V_D/1000}{\sqrt{cos(\Lambda_{v,0.5})}} \tag{D.12}$$

The function $f_{y(x)}$ is computed by a curve fit to Figure 8-5 of [44]:

$$f_y(x) = -640.4x^6 + 2844.4x^5 - 4120x^4 + 2612.8x^3 - 816.11x^2 + 186.21x - 10.277 \tag{D.13}$$

Acknowledgements

First of all, I want to thank Javier Hilario for his trust. He supported me in the accomplishment of this project and gave me the chance to work for a year at his department in Airbus Defence & Space. I could never had a better example of passion about doing what you really love.

These past years at university changed my life. I want to publicly thank University Carlos III for having the opportunity of studying abroad at University of Maryland and University of Sydney. I would never changed the experiences around the world and the friends I made. No words can describe those feelings.

I thank my family for its continuous care and encouragement. Thanks to my father, for instilling me the values of effort and sacrifice in life. To my mother, for always showing me her positive way of facing life. And to my brother and sister, for being guilty of countless laughing moments. They all made me the person I am today.

And finally, but no less important, thanks to those special people who have advised me in life, that they helped me to overcome challenges and overall, they taught me to fight. Thanks to my friends.

This page intentionally left blank.